nature communications

Article

https://doi.org/10.1038/s41467-025-67579-7

Agonist signaling drives neutrophil subpopulations to promote/inhibit colorectal cancer liver metastasis

Received: 25 March 2025

Accepted: 3 December 2025

Published online: 17 December 2025

Check for updates

Zhuoqing Xu[1,2,3,7], Haoran Feng[1,2,3,7], Wenqing Feng[1,3,4,7], Yuchen Zhang[1,3,5,7], Jianting Huo[1,3,5], Zifeng Xu[1,3], Fangqian Chen[1,3], Han Gao[1,3,5], Zeping Lv[1,3,5], Wangyi Liu[1,3,5], Abudumaimaitijiang Tuersun[1,3,5], Suyue Yu[1,3,5], Wenchang Li[3,6], Yaping Zong[1,5], Xiaohui Shen[1,4] ✉, Xi Cheng[1,2,3] ✉, Jingkun Zhao[1,5] ✉ & Aiguo Lu[1,5] ✉

Liver metastasis is a primary cause of death in colorectal cancer, yet the role of immune cells called neutrophils in this process remains complex. In this study, we identify three distinct neutrophil subtypes: anti-tumor high-density neutrophils, pro-tumor mature low-density neutrophils, and immature low-density neutrophils. Here we show that tumor-derived GM-CSF converts anti-tumor neutrophils into a pro-tumor state via the AKT–NF-κB–NFAT5 signaling axis. These activated neutrophils, when further stimulated by CXCR2 ligands, release web-like structures known as neutrophil extracellular traps which promote cancer spread by enhancing cancer cell growth, suppressing immune responses, and preparing the liver for metastasis. Importantly, we demonstrate that using antibodies depleting neutrophils or drugs inhibiting their pro-tumor activity effectively reduces liver metastasis in mice. Our work defines specific neutrophil subsets as key drivers of cancer progression and highlights their therapeutic potential in preventing metastatic spread.

In recent years, numerous advances in the diagnosis and treatment of colorectal cancer (CRC) have been made; however, the associated mortality rate remains very high[1]. Distant metastases, especially liver metastases, are the leading causes of death in patients with CRC[2]. Malignant tumor cells metastasize to distant organs through a complex series of steps, including invasion, circulation in vivo, extravasation, and colonization, which are driven by both the intrinsic and extrinsic factors of the tumor[3–6]. Our previous studies have shown that the chemokine—CXCL5—is overexpressed in CRC and is associated with distant metastasis and that CXCL5 promotes liver metastasis by promoting the migration and invasion of CRC cells and tumor angiogenesis[7,8]. CXCL5, an epithelial-derived neutrophil-activating peptide[9], is crucial in the recruitment and regulation of neutrophil function in the tumor microenvironment (TME)[10–13].

Neutrophils play an important role in tumor progression and distant metastasis[14,15]. Neutrophils reportedly accumulate in the peripheral blood of patients with advanced tumors, and a high circulating neutrophil-to-lymphocyte ratio is a reliable biomarker for the poor prognosis of various cancers[16]. Neutrophils support metastasis

[1]Department of General Surgery, Ruijin Hospital, Shanghai Jiaotong University School of Medicine, Shanghai, PR China. [2]Institute of Medical Robotics, Ruijin Hospital, Shanghai Jiao Tong University School of Medicine, Shanghai, PR China. [3]Shanghai Institute of Digestive Surgery, Shanghai, PR China. [4]Department of General Practice, Ruijin Hospital, Shanghai Jiaotong University School of Medicine, Shanghai, PR China. [5]Shanghai Minimally Invasive Surgery Center, Ruijin Hospital, Shanghai Jiaotong University School of Medicine, Shanghai, PR China. [6]Department of Radiology, Ruijin Hospital, Shanghai Jiaotong University School of Medicine, Shanghai, PR China. [7]These authors contributed equally: Zhuoqing Xu, Haoran Feng, Wenqing Feng, Yuchen Zhang.
✉e-mail: xhshendoc@yeah.net; drchengxi@126.com; zhaojk8891@126.com; luaiguo1965@163.com

progression by releasing immunomodulators, growth factors, inflammatory mediators, proteases, and neutrophil extracellular traps (NETs)[17–20]. Conversely, neutrophils have been evidenced to limit malignant progression through direct tumor cytotoxicity or activation of cells with anti-tumor functions[21–24]. Therefore, the role of neutrophils in cancer has been debated, in addition to the hypothesis that the presence of tumors could affect neutrophil activity and function[25–27].

Given the complex role of neutrophils in cancer, herein, we distinguished three neutrophil subgroups in patients and mice with CRC, namely high-density neutrophils (HDNs), mature low-density neutrophils (M-LDNs), and immature low-density neutrophils (IM-LDNs). We comprehensively evaluated the surface marker characteristics, gene expression levels, biological functions, and micromorphology of the three neutrophil subsets. Additionally, we sought to understand the interactions among neutrophils, CRC cells, and other anti-tumor immune cells. Furthermore, we explored the potential of targeting neutrophils and their two activation processes in CRC therapy. Our study has important implications, as it offers insights on "double-edged-sword" role of neutrophils in cancer.

Results

CXCL5 promotes CRC liver metastasis by recruiting neutrophils in vivo

The CXCL5-CXCR2 axis drives CRC liver metastasis[7,8], with neutrophil involvement supported by existing evidence[28,29]. Analysis of TIMER database revealed positive correlations between *CXCL5*/*CXCR2* expression and neutrophil infiltration across malignancies, including CRC (Fig. S1A–F). GEPIA data further demonstrated *CXCL5*/*CXCR2* co-expression with neutrophil-associated genes (*CD16*, *S100A9*, *CSF3R*, *ITGAM*, *CD33*, *OLR1*) in CRC (Fig. S1G). TCGA and CPTAC analysis confirmed associations between neutrophil marker expression, CRC progression, and poor prognosis (Fig. S2A–E). A tissue microarray of 78 pairs of CRC and adjacent normal intestinal tissues[7] showed CXCL5/CXCR2 expression positively correlated with $CD66b^+MPO^+$ neutrophil infiltration (Fig. S3A–H). Consistently, immunohistochemical (IHC) analysis of paired CRC liver metastasis specimens revealed elevated CXCL5 expression and neutrophil density in both primary tumors and metastatic tissues (Fig. S3I, J).

Using CT26 mouse models, we found CXCL5 knockdown (sh-CXCL5) significantly inhibited colon cancer growth and liver metastasis in immunocompetent BALB/c mice, while suppressing only liver metastasis in T-cell-deficient nude mice (Fig. 1A, S4A–D). Neutrophil infiltration (labeled by CD11b/LY6G/S100A9 staining) was markedly reduced in sh-CXCL5 tumors and liver metastases (Fig. 1B, S4E-G). Subsequent anti-Ly6G-mediated neutrophil depletion further suppressed metastatic progression (Fig. 1C, S4H), confirming that CRC-derived CXCL5 promotes liver metastasis through neutrophil recruitment.

CRC cells recruit and activate neutrophils through CXCR2 ligands in vitro

Given CRC cells recruit neutrophils in vivo (Fig. S4I, J), we investigated their effects on neutrophils in vitro. Neutrophils isolated from CRC patient peripheral blood were used, as tumors typically recruit circulating neutrophils to the TME[30]. Both CRC cell-conditioned medium (CM) and CXCL5 induced neutrophil chemotaxis (Fig. 1D, E, S4K). SB225002 (CXCR2 inhibitor) completely blocked CRC-induced neutrophil migration, while anti-CXCL5 neutralizing antibodies only partially inhibited it (Fig. 1F), suggesting additional CXCR2 ligands contribute to recruitment. UALCAN analysis confirmed high expression levels of *CXCL1, CXCL2, CXCL3, CXCL6*, *CXCL7*, and *CXCL8* in CRC (Fig. S5A), and TIMER data revealed their positive correlations with neutrophil infiltration in solid tumors (Fig. S5B, C). Finally, CXCL5/6/8-induced chemotaxis was verified in vitro (Fig. 1G).

NETosis, a distinct form of neutrophil death inducible by external stimuli and implicated in tumor progression[27,31], was quantified by measuring extracellular NETs release using SYTOX Green staining. CRC cells effectively induced neutrophil activation and NETosis (Fig. 1H), and this process was blocked by SB225002 (Fig. 1I). Single CXCR2 ligands (5 ng/mL) failed to trigger NETosis (Fig. 1J), but high concentrations (20 ng/mL) of CXCL5/6/8 significantly induced NETosis in stage III–IV CRC neutrophils (Fig. 1K), consistent with known concentration-dependent responses[29]. This differential responsiveness to CXCR2 ligands across tumor stages prompted us to characterize neutrophil heterogeneity across CRC progression stages.

Three neutrophil types are present in patients and mice with CRC

Previous studies have reported a classification method for neutrophil subpopulations defined by the density gradient[26,32]. Dual-density centrifugation divided cells into three layers: low-density layer (rich in LDNs), high-density layer (rich in HDNs), and red blood cell (RBC) layer (Fig. 2A). Analysis of CRC patient peripheral blood revealed increased low-density neutrophils in stage III–IV versus stage I–II patients (Fig. 2B). Microscopically, nuclear morphology distinguished immature (IM-LDN; lobular nucleus) and mature LDNs (M-LDN; segmented nucleus) in low-density layer, while HDNs were uniformly mature (Fig. 2C). Flow cytometry was then used to detect the cell subsets in each layer, selecting the granulocyte marker (CD11b), monocyte marker (CD14), and neutrophil maturation markers (CD66b, CD10) as the detection indices. The results showed that the high-density layer contained mature HDNs ($CD14^-CD11b^+CD66b^+CD10^+SSC^{high}FSC^{high}$), whereas the low-density layer contained M-LDN ($CD14^-CD11b^+CD66b^+CD10^+SSC^{high}FSC^{high}$), monocytes ($CD14^+CD11b^+CD66b^-CD10^-SSC^{low}FSC^{mid}$), and IM-LDN ($CD14^-CD11b^+CD66b^-CD10^-SSC^{low}FSC^{low}$) (Fig. 2D, E). Analysis of 30 patients demonstrated significantly increased M-LDN proportions during tumor progression, with stable HDN/IM-LDN levels (Fig. 2F, S6A).

The orthotopic CRC model with spontaneous metastasis was established using Microsurgical Implantation (MSOI) method[33] (Fig. S6B). Peripheral blood from CRC mice was also analyzed, and the three types of neutrophils (HDNs, M-LDNs, and IM-LDNs) were observed under a microscope (Fig. 2G). Flow cytometry confirmed that both HDNs and M-LDNs expressed neutrophil markers CD11b and Ly6G, while $CD11b^+Ly6G^-$myeloid cells were distinctly identified (Fig. 2H, I). Neutrophil subset distributions in peripheral blood were assessed across four groups: normal controls, early-stage CRC, advanced-stage CRC, and liver metastasis-bearing mice. HDN and M-LDN proportions progressively increased with tumor progression (Fig. 2J).

Next, neutrophils in the tumor tissues from patients with CRC were detected. Microscopy and flow cytometry confirmed the presence of $CD11b^+CD66b^+$ M-LDN and $CD11b^+CD66b^+$ HDN (Fig. 2K, L). M-LDNs showed elevated CD11b/CD66b but reduced CD16/CD10 versus HDNs (Fig. S6C). Multispectral IHC (mIHC) of CRLM tissues showed HDNs predominant in normal intestine, M-LDNs dominant in CRC and metastatic liver tissues, and both HDN and M-LDN were identified in the adjacent liver tissues (Fig. 2M). With tumor progression, HDN and M-LDN infiltration in the CRC tissues significantly increased (Fig. 2N, S6D). Similar to the results in human CRC, $CD11b^+Ly6G^+$ M-LDNs and $CD11b^+Ly6G^+$ HDNs were identified in mouse colon cancer tissues (Fig. 2O, P).

HDNs exhibit anti-tumor properties while M-LDNs display pro-tumor characteristics

Neutrophil heterogeneity between circulation and TME can be analyzed using specific biomarkers[34,35]. We purified HDNs, M-LDNs, and IM-LDNs from CRC patient peripheral blood via magnetic bead sorting,

https://doi.org/10.1038/s41467-025-67579-7

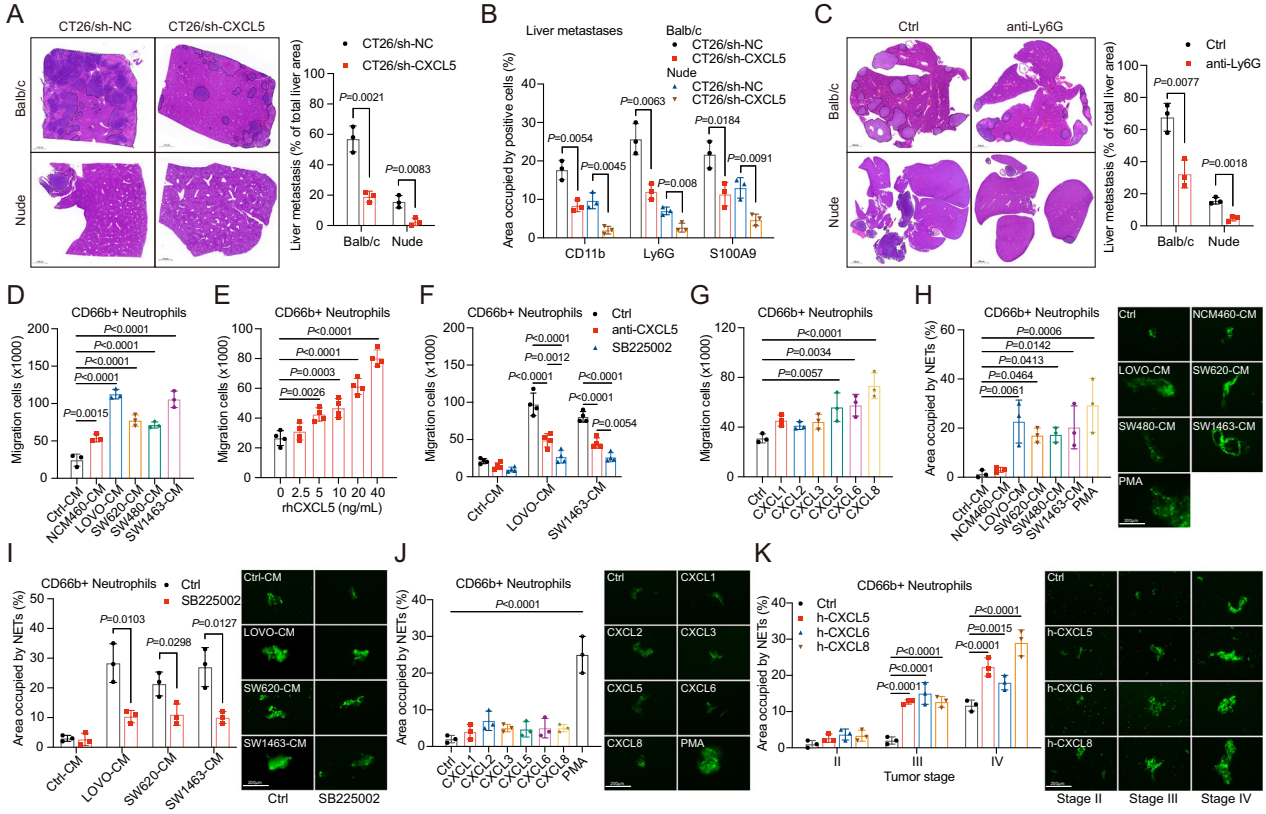

Fig. 1 | Colorectal cancer (CRC) cells recruit and activate neutrophils both in vivo and in vitro, in part through CXCR2 ligands. Knockdown of CXCL5 expression in colon cancer cells significantly inhibited liver metastases (**A**) and neutrophil infiltration (**B**) in Balb/c mice and nude mice. Scale bars, 1000 μm. n = 3, data were presented as mean ± SD, two-tailed unpaired T-test. **C** Neutrophil depletion by anti-Ly6G significantly inhibited colon cancer liver metastases in Balb/c mice and nude mice. Scale bars, 1000 μm. n = 3, data were presented as mean ± SD, two-tailed unpaired T-test. **D** The migration assay showed that the culture medium (CM) from human colon epithelial cells NCM460 and CRC cell lines (LOVO, SW620, SW480, SW1463) significantly recruited neutrophils. n = 3 for each group, data were presented as mean ± SD, one-way ANOVA. **E** The migration assay demonstrated CXCL5-induced neutrophil recruitment in a concentration-dependent manner (stimuli concentrations indicated). n = 4, data were presented as mean ± SD, one-way ANOVA. **F** The migration assay revealed that CXCR2 inhibition (SB225002, 10 nM) completely prevent neutrophil chemotaxis toward CRC cells, while anti-CXCL5 neutralizing antibodies (10 μg/mL) partially inhibited chemotaxis. n = 4, data were presented as mean ± SD, two-way ANOVA. **G** The migration assay confirmed that CXCL5, CXCL6, and CXCL8 (5 ng/mL) recruited neutrophils effectively in vitro. n = 3, data were presented as mean ± SD, one-way ANOVA. **H** NETosis analysis indicated that CM from CRC cell lines effectively activate neutrophils to release NETs. PMA (25 ng/mL) was used as positive control. Scale bars, 200 μm. n = 3, data were presented as mean ± SD, one-way ANOVA. **I** NETosis analysis showed that CXCR2 inhibitor (SB225002, 10 nM) effectively prevent NETosis development. Scale bars, 200 μm. n = 3, data were presented as mean ± SD, two-tailed unpaired T-test. **J** CXCR2 ligands (5 ng/mL) did not effectively activate neutrophil NETosis. PMA (25 ng/mL) was used as positive control. Scale bars, 200 μm. n = 3, data were presented as mean ± SD, one-way ANOVA. **K** High concentrations of CXCL5, CXCL6, and CXCL8 (20 ng/mL) significantly activated NETosis in neutrophils from stage III-IV CRC patients. Stimuli concentrations as in Supplementary Data. 2, PMA (25 ng/mL) as positive controls. Scale bars, 200 μm. n = 3, data were presented as mean ± SD, two-way ANOVA. See also Figs. S1–5. Source data are provided as a Source Data file.

with efficiency validated by flow cytometry and microscopy (Fig. S7A-C). Flow cytometry was used to detect the expression of cell surface markers, and revealed that IM-LDNs lacked maturation markers (CD66b/CD15/CD16/CD10/CXCR2) compared with mature neutrophils (Fig. 3A, S7D). M-LDNs showed elevated maturation markers (CD11b/CD66b/CD15) and G-MDSC markers (CD274/LOX-1) with consistent expression across CRC stages (Fig. S7E).

Gene expression profiles of HDNs, M-LDNs, and IM-LDNs were determined using Digital RNA with Perturbation of Genes (DRUG-seq), showing strong intra-subset consistency across CRC patient sources (Fig. 3B, S8A). Correlation analysis with five independent studies[36–40] demonstrated alignment between our neutrophil states and published tumor-infiltrating neutrophil subpopulations (Fig. 3C, S8B). Single-cell RNA sequencing (scRNA-seq) of 11 CRC tumor tissues was performed, followed by dimensionality reduction and neutrophil clustering. After the correction of batch effect, six neutrophil subclusters were identified (Fig. 3D, S8C, D, F). These subclusters correlated with our neutrophil subsets: HDNs with Neutrophils_S100A12, M-LDNs with Neutrophils_LCN2, and IM-LDNs with Neutrophils_IGHG3 (Fig. 3E). Differentiation trajectories suggested Neutrophils_LCN2 derivation from Neutrophils_S100A12 (Fig. S8E). Gene-set variation analysis revealed Neutrophils_LCN2 enrichment in oxidative phosphorylation genes and Neutrophils_S100A12 in T-cell activation genes (Fig. S8G). These results suggested that HDNs, M-LDNs, and IM-LDNs in the peripheral blood from CRC patients were highly similar to tissue-infiltrating neutrophils, and that HDNs and M-LDNs may have different functions in terms of oxidative burst and T cell activation.

The functions of the neutrophils include chemotaxis, phagocytosis, antitumor activity, immunosuppression, oxidative stress, degranulation, and NETosis[26,41]. Chemotaxis assays revealed HDNs exhibited strongest migration toward CRC cells and normal intestinal epithelial cells (NCM460), while M-LDNs showed partial chemotaxis to CRC cells and IM-LDNs had no chemotaxic property (Fig. 3F). Phagocytic capacity was retained in HDNs and M-LDNs but absent in IM-LDNs (Fig. 3G). Co-culture experiments demonstrated only HDNs killed and induced apoptosis in CRC cells (Fig. 3H, I, S9A), whereas M-LDNs uniquely suppressed T-cell proliferation and antitumor function (Fig. 3J, K). Oxidative stress analysis showed that M-LDNs

https://doi.org/10.1038/s41467-025-67579-7

released high H_2O_2 into CM (Fig. 3L), M-LDNs mainly produced ROS, and HDNs mainly produced mitochondrial ROS (Fig. 3M, N). M-LDNs were more prone to higher levels of NETosis than HDN and IM-LDN (Fig. 3O). Oxidative bursts and NETosis inducers were used to pre-treat neutrophils to measure the ability of neutrophil subsets to respond to external stimuli. HDNs responded to PMA, ionomycin, and LPS to produce H_2O_2 and mitochondrial ROS, whereas M-LDNs were mainly stimulated by PMA to produce ROS and release H_2O_2 into the CM (Fig. 3P, S9B-D). PMA, ionomycin, and LPS could induce HDN and M-LDNs undergoing NETosis (Fig. 3Q), demonstrating shared responsiveness to external stimuli.

Neutrophil granules include elastase (NE), azurocidin (AZU), myeloperoxidase (MPO), and cathepsin G (CG)[42,43]. Enzyme-linked immunosorbent assay (ELISA) measured granule protein levels in HDN- and M-LDN-CM, revealing greater particle release from HDNs. HDNs secreted NE, MPO, AZU, and CG, while M-LDNs primarily released MPO and AZU (Fig. 3R). Electron microscopy showed HDNs as spherical with abundant cytoplasmic particles, whereas M-LDNs appeared elliptical with reduced particles (Fig. 3S). CRC cell line SW620 was used to construct liver metastasis model in nude mice, adoptively transferred HDNs inhibited metastases while M-LDNs promoted them (Fig. 3T, S9E, F). These results suggest that HDNs may predominantly function as anti-tumor neutrophils, while M-LDNs appear to exhibit pro-tumor properties. Given that the degranulation process of HDNs may potentially contribute to the formation of pro-tumor neutrophil pools, we next examined the

https://doi.org/10.1038/s41467-025-67579-7

Fig. 2 | Patients and mice with colorectal cancer (CRC) have three different types of neutrophils. A Cells were separated into three distinct layers via dual-density Histopaque centrifugation (1077/1119). Top to bottom were low-density layer, high-density layer, and red blood cell (RBC) layer, respectively. **B** Microscopic images showed that the low-density layers in the blood from patients with stage III-IV CRC were rich in neutrophils. Scale bars, 200 μm. **C** Based on the morphology of the nucleus, low-density neutrophils (LDNs) comprised immature neutrophils (IM-LDNs) and mature neutrophils (M-LDNs), while the high-density neutrophils (HDNs) were uniformly mature. Scale bars, 200 μm. **D** The low-density layer contained three cell populations: M-LDNs ($CD14^-CD11b^+CD66b^+CD10^+SSC^{high}FSC^{high}$), monocytes ($CD14^+CD11b^+CD66b^-CD10^-SSC^{low}FSC^{mid}$), and IM-LDNs ($CD14^-CD11b^+CD66b^-CD10^-SSC^{low}FSC^{low}$). **E** The high-density layer contained HDNs ($CD14^-CD11b^+CD66b^+CD10^+SSC^{high}FSC^{high}$). **F** During tumor progression, the proportions of HDNs and IM-LDNs did not significantly change, while the proportion of M-LDNs significantly increased. n = 6, data were presented as mean ± SD, one-way ANOVA. **G** Microscopic examination of peripheral blood from mice with CRC liver metastases revealed M-LDNs and IM-LDNs in the low-density layer, and HD in the high-density layer. Scale bars, 200 μm. **H, I** The low-density layer contained M-LDNs ($CD11b^+Ly6G^+SSC^{high}FSC^{high}$) and $CD11b^+Ly6G^-$myeloid cells ($CD11b^+Ly6G^-SSC^{low}FSC^{low}$), while the high-density layer included HDNs ($CD11b^+Ly6G^+SSC^{high}FSC^{high}$). **J** Orthotopic CRC spontaneous metastasis model was established by Microsurgical Implantation, and mice were divided into healthy controls, early-stage CRC, advanced-stage CRC, and liver metastasis groups based on tumor progression timeline. During tumor progression, the proportion of $CD11b^+Ly6G^-$myeloid cells decreased, while the proportion of HDNs and M-LDNs significantly increased. n = 7, data were presented as mean ± SD, one-way ANOVA. **K, L** The tumor tissue from patients with CRC contained M-LDNs ($CD16^+CD11b^+CD66b^+CD10^+SSC^{high}FSC^{high}$) and HDNs ($CD16^+CD11b^+CD66b^+CD10^+SSC^{high}FSC^{high}$). Scale bars, 200 μm. **M** Multiplex immunohistochemical (mIHC) analysis revealed HDNs predominance in healthy intestinal tissues, M-LDN predominance in CRC and liver metastases, and coexistence of both HDN and M-LDN in metastasis-adjacent normal liver tissues. Scale bars, 200 μm. **N** During tumor progression, the proportion of HDNs and M-LDNs significantly increased. n = 3, data were presented as mean ± SD, one-way ANOVA. **O, P** The tumor tissue from the liver metastases mice contained M-LDNs ($CD11b^+Ly6G^+SSC^{high}FSC^{high}$) and HDNs ($CD11b^+Ly6G^+SSC^{high}FSC^{high}$). Scale bars, 200 μm. Data shown in Fig. 2B, C, G, K, M, and O are representative of three independent experiments. See also Figure S6. Source data are provided as a Source Data file.

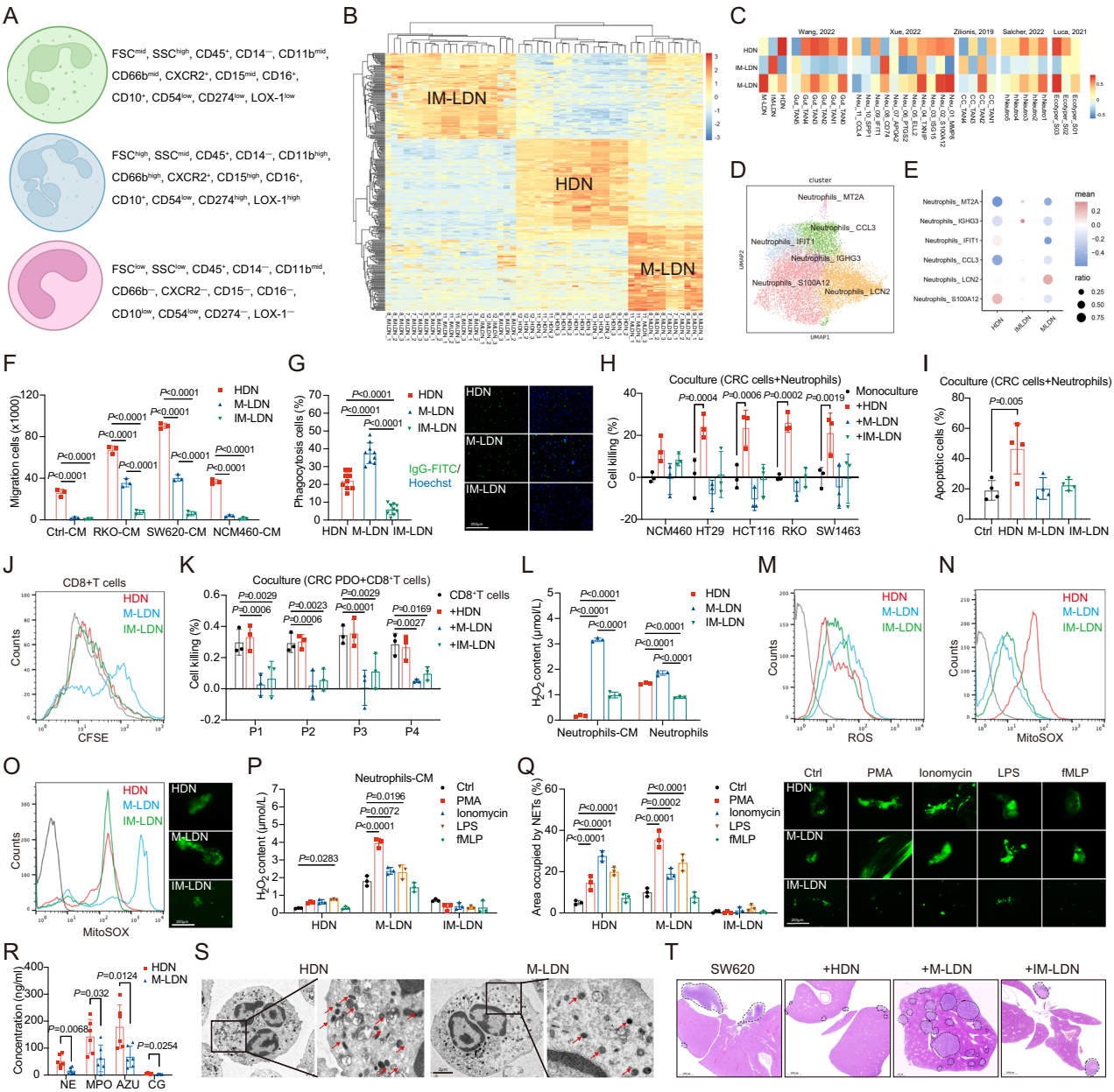

Fig. 3 | Functional and gene expression characteristics of three neutrophil subsets in colorectal cancer (CRC) patients. A Surface marker expression profiles of three neutrophil subsets. Created in BioRender. Guo, Z. (2025) https://BioRender.com/1ay5uxr. **B** DRUG-seq analysis of HDNs, M-LDNs, and IM-LDNs from the peripheral blood of CRC patients. Heatmap shows upregulated genes. **C** Comparison of three neutrophil subsets from the peripheral blood samples in this study with published human neutrophil states. **D** The scRNA-seq of 11 CRC tumor tissues (GSE302903), and UMAP plots displayed the six neutrophil subsets in the CRC tissues. **E** Comparisons among three neutrophil subsets from peripheral blood with six neutrophil subsets from the tumor tissues of patients with CRC. **F** The migration assay showed that HDNs exhibited the highest chemotaxis toward both CRC and healthy intestinal epithelial cells, M-LDNs showed partial chemotaxis toward CRC cells, whereas no chemotaxis was observed for IM-LDNs. n = 3, data were presented as mean ± SD, two-way ANOVA. **G** Phagocytosis assay showed M-LDNs exhibited higher phagocytic ability than HDNs, whereas IM-LDNs retained no phagocytic function. Scale bars, 200 μm. n = 9, data were presented as mean ± SD, one-way ANOVA. **H** The killing assay showed that HDNs were cytotoxic to CRC cells in a coculture environment, whereas M-LDN and IM-LDN did not show any cytotoxic effects. n = 3, data were presented as mean ± SD, two-way ANOVA. **I** The apoptosis detection showed that HDNs induced apoptosis in CRC cells in a coculture environment, whereas M-LDNs and IM-LDNs did not. n = 4, data were presented as mean ± SD, one-way ANOVA. **J** CFSE staining was used to evaluate the proliferation of T cells, and the fluorescence of the proliferating cells was reduced. M-LDNs inhibited T-cell proliferation, whereas HDNs and IM-LDNs did not. **K** $CD8^+$T cells were pretreated with neutrophils and then co-cultured with CRC patient-derived organoids (PDOs). The killing assay showed that activated CD8 T were toxic to CRC PDOs. M-LDN and IM-LDN significantly inhibited the T-cell killing of CRC PDOs, whereas HDNs exhibited no such effect. n = 3, data were presented as mean ± SD, two-way ANOVA. **L** The H_2O_2 content in the cell culture medium (CM) and the lysate of neutrophils were detected, M-LDNs released high H_2O_2 into the CM. n = 3, data were presented as mean ± SD, two-way ANOVA. **M**, **N** The oxidative stress level analysis showed that M-LDNs mainly produced and released reactive oxygen species (ROS), whereas HDNs mainly produced and released mitochondrial ROS. **O** SYTOX Green was used to measure NET release to assess NETosis rate in neutrophils. M-LDNs were more prone to high rate of NETosis. Scale bars, 200 μm. **P** M-LDNs were more prone to release H_2O_2 into the CM when induced by PMA (25 ng/mL), ionomycin (5 μM), or LPS (100 ng/mL). n = 3, data were presented as mean ± SD, two-way ANOVA. **Q** NETosis was induced in HDNs and M-LDNs using PMA (25 ng/mL), ionomycin (5 μM), and LPS (100 ng/mL). Scale bars, 200 μm. n = 3, data were presented as mean ± SD, two-way ANOVA. **R** The content of granular constituents in the CM of HDN and M-LDN were analyzed using ELISA. HDNs can release more particles than M-LDNs. HDNs secreted NE, MPO, AZU, and CG, whereas M-LDNs mainly secreted MPO and AZU. n = 6, data were presented as mean ± SD, two-tailed unpaired T-test. **S** The electron microscope showed the intracellular structure. HDN was spherical, and the cytoplasmic particles were large, whereas M-LDN was oblong with smaller cytoplasmic particles. Data are representative of three independent experiments. Scale bars, 2 μm. **T** CRC cell line, SW620, was used to construct liver metastasis model in nude mice. HDN treatment inhibited liver metastases, whereas M-LDN promoted liver metastases. Data are representative of three independent experiments. Scale bars, 2000 μm. Stimuli concentrations as in Supplementary Data. 2. See also Figure S7–9. Source data are provided as a Source Data file.

ability of CRC cells to transform HDNs into M-LDNs and the associated regulatory mechanisms.

GM-CSF promotes HDN-mediated tumor cell killing and drives phenotypic conversion toward M-LDN

Given tumor microenvironments mimic chronic inflammation[44], neutrophil subsets were analyzed in inflammatory conditions. Both human inflammatory patients and LPS-treated mice showed increased M-LDN proportions versus controls (Fig. S10A-J). As inflammatory conditions activate neutrophils and induce degranulation[45], we propose tumor-derived stimuli may trigger HDN degranulation and drive their phenotypic conversion toward M-LDN (Fig. 4A). To identify activating molecules, CRC cell line CM was screened for HDN activation capacity using tumor-killing assays (Fig. 4B, S11A). Surface marker changes (CD11b/CD66b/LOX-1/CD274) and ROS production served as conversion indicators (Fig. S11B). Based on the detection of the various indicators, CT26, SW480, LOVO, SW48, HT29, SW620, and SW1463 were defined as HDN-activated CRC cells, whereas Caco2, DLD1, RKO, SW1116, and HCT116 were defined as non-HDN-activated CRC cells (Fig. 4C, S11C).

Luminex analysis showed high secretion of eight proteins in the CM of the HDN-activated CRC cells (Fig. S11D, Supplementary Data 6), and microarray analysis showed high secretion levels for 11 proteins (Fig. 4D, Supplementary Data 7). The CCLE database showed high expression levels of five genes in the HDN-activated CRC cells (Fig. S11E). Integration revealed seven candidate activators: GM-CSF, BMP4, IL-1β, CXCL6, CCL15, CCL24, and IGFBP4 (Fig. 4E). Functional validation confirmed only GM-CSF activated HDN-to-M-LDN conversion, enhancing tumor-killing (Fig. 4F), upregulating surface markers (CD11b/CD66b/LOX-1/CD274), inducing mitochondrial ROS, and elevating M-LDN signature genes' expression (Fig. 4G, H). Anti-GM-CSF blocked CRC-CM-induced HDN activation (Fig. 4I, S11F, G). Public datasets (GSE166555, EMTAB8107, and GSE146771) showed GM-CSF expression in macrophages, T cells, B cells, fibroblasts, and epithelial cells (Fig. S11H). mIHC staining showed that GM-CSF co-localized with the CRC cell-specific marker EpCAM (Fig. S11I).

HDN activation can cause the release of ROS, mitochondrial ROS, degranulation, and NETs, all of which reportedly have lethal effects[23,24]. Activated HDNs were fractionated into cell precipitate, NETs, and CM, with CM mediating primary anti-tumor activity (Fig. 4J). Pretreatment with MitoTEMPO (mitochondria-targeting antioxidant) and Nexinhib20 (degranulation inhibitor) reversed the anti-tumor effect of HDN (Fig. 4K), confirming its mitochondrial ROS and degranulation dependency. Electron microscopy visualized GM-CSF-enhanced degranulation (Fig. 4L). Ultrafiltration centrifugation of HDN CM showed >10 kDa, >30 kDa, and <100 kDa components killed CRC cells (Fig. 4M). Per manufacturer data, effective proteins approximated 30 kDa; prior studies note NE, AZU, and CG at ~30 kDa versus MPO at 80 kDa. ELISA confirmed GM-CSF-induced NE, AZU, and CG release (Fig. S12A). Recombinant human AZU and NE proteins confirmed cytotoxic effects in vitro (Fig. 4N, S12B), demonstrating that HDN-mediated CRC cell killing primarily involves mitochondrial ROS and degranulation products AZU/NE.

Next, we assessed the effect of targeted inhibition of GM-CSF on liver metastasis in vivo. Anti-GM-CSF neutralizing antibodies promoted CRC liver metastasis in mice (Fig. 4O, S12C). While GM-CSF targeting didn't affect total neutrophil recruitment to metastases, it significantly reduced MPO^+ neutrophil infiltration in liver metastasis and decreased blood M-LDN proportions and NETs concentrations (Figs. S12D, E, S17F-I). To directly visualize HDN-mediated tumoricidal effects in vivo, we conducted complementary studies in T cell-deficient nude mice. Local intratumoral injection of HDNs significantly suppressed SW620 subcutaneous tumor growth in neutrophil-depleted nude mice pretreated with anti-Ly6G (Fig. S12F, G). Although anti-Ly6G monotherapy suppressed CRC progression, suggesting net pro-tumor neutrophil activity in vivo, and GM-CSF increased M-LDN proportions in CRC, these effects were insufficient to reverse the dominant anti-tumor outcome resulting from GM-CSF-induced HDN activation (Fig. S12H-I).

GM-CSF induces the conversion of HDN to M-LDN through the AKT/NF-κB/NFAT5 axis

To identify gene expression changes in GM-CSF-activated HDN, we performed DRUG-seq (Fig. 5A, B). KEGG pathway analysis of differentially expressed genes after GM-CSF treatment identified enrichment in PPARγ, PI3K-Akt, and NF-κB signaling pathways (Fig. 5C). GM-CSF upregulated RNA expression of transcription factors *PPARG, XBP1, NFAT5*, and *BHLHE40* (Fig. 5D), with protein-level validation showing

https://doi.org/10.1038/s41467-025-67579-7

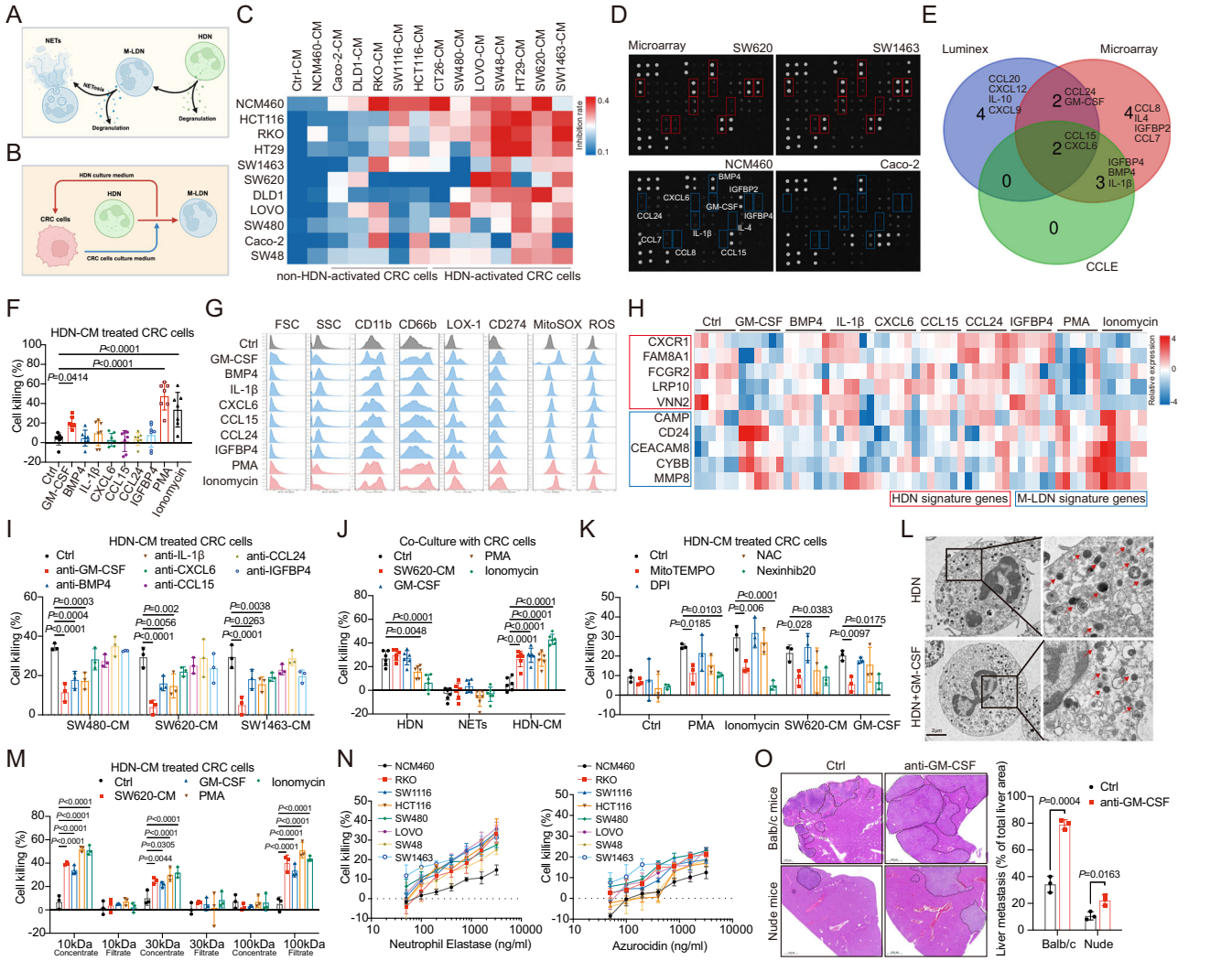

Fig. 4 | GM-CSF induced HDNs to kill colorectal cancer (CRC) cells and transform HDNs into M-LDNs. A Hypothesis diagram showing how CRC cells activate HDNs to induce degranulation and their transformation into M-LDNs, followed by re-degranulation and NETosis of M-LDNs. Created in BioRender. Guo, Z. (2025) https://BioRender.com/dcwuy59. **B** Experimental design: culture medium (CM) from different CRC cell lines was used to culture HDNs, and then HDN-CM was collected to treat CRC cells. HDN activation was evaluated by the killing effect of HDN-CM on CRC cells, identifying CRC cell lines capable of effectively activating HDNs (HDN-activated CRC cells). **C** Killing assay: CT26, SW480, LOVO, SW48, HT29, SW1463, and SW620 potently activated HDNs and are defined as HDN-activated CRC cells. Caco2, DLD1, RKO, SW1116, and HCT116 did not effectively activate HDNs and are defined as non-HDN-activated CRC cells. **D** Microarray analysis showed elevated levels of 11 proteins (CCL8, IL4, IGFBP2, CCL7, CCL24, GM-CSF, CCL15, CXCL6, IGFBP4, BMP4, IL-1β) in the CM for the HDN-activated CRC cells (SW620 and SW1463). **E** Venn diagram identified seven HDN-activating candidates: CCL24, GM-CSF, CCL15, CXCL6, IGFBP4, BMP4, and IL-1β. **F** GM-CSF significantly induce the anti-tumor function of HDNs versus other candidates. n = 7, data were presented as mean ± SD, one-way ANOVA. **G** GM-CSF upregulated M-LDN surface markers (CD66b, CD11b, CD274, LOX-1) expressions and mitochondrial ROS production in HDNs. **H** GM-CSF downregulated HDN signature genes but upregulated M-LDN signature genes in HDNs. **I** Anti-GM-CSF, anti-BMP4, and anti-IL-1β antibodies inhibited CRC-CM-induced HDN activation. n = 3, data were presented as mean ± SD, two-way ANOVA. **J** HDNs were fractionated into three components: cell precipitation, NETs, and CM. The anti-tumor functions of activated HDNs were primarily mediated through HDN-CM, whereas NETs conversely promoted CRC cell proliferation. n = 6, data were presented as mean ± SD, two-way ANOVA. **K** MitoTEMPO (mitochondria-targeted antioxidant) and Nexinhib20 (neutrophil degranulation inhibitor) blocked antitumor effects of HDNs. n = 3, data were presented as mean ± SD, two-way ANOVA. **L** Electron microscopy showed the intracellular structure of HDNs, and GM-CSF stimulation reduced cytoplasmic granules in HDNs. Data are representative of three independent experiments. Scale bars, 2 μm. **M** The results of killing assay. In the CM of activated HDN, components with molecular weights >10 kDa, >30 kDa, and <100 kDa significantly killed CRC cells. n = 3, data were presented as mean ± SD, two-way ANOVA. **N** Human recombinant AZU and NE had dose-dependent killing effects on CRC cells in vitro. **O** CT26 was used to establish a liver metastasis model in BALB/c and nude mice. Anti-GM-CSF antibody treatment significantly promoted liver metastases. Scale bars, 1000 μm. n = 3, data were presented as mean ± SD, two-tailed unpaired T-test. Stimuli concentrations: GM-CSF (10 ng/mL); others as in Supplementary Data. 2; PMA (25 ng/mL)/ionomycin (5 μM) as positive controls. See also Figure S10–12 and Supplementary Data. 6, 7. Source data are provided as a Source Data file.

increased expression and activation of XBP1, NFAT5, and p65 (NF-κB) (Fig. 5E, S13S). Pretreatment with B-I09 (IRE-1 RNase inhibitor), KRN2 (NFAT5 inhibitor), and BAY11-7082 (NF-κB inhibitor) blocked HDN-to-M-LDN, evidenced by suppressed upregulation of CD11b/CD66b/LOX-1/CD63, reducing mitochondrial ROS, downregulating M-LDN signature genes, and enhancing HDN anti-tumor function (Fig. 5F-H).

Neutrophil extracellular stimulation signals are reportedly transmitted downstream through specific receptors to activate MAPK, PI3K, and other pathways[46–49]. GM-CSF upregulated the phosphorylation levels of AKT and mTOR in HDNs (Fig. 5I, S13B). LY294002 (PI3K inhibitor) and AZD5363 (AKT inhibitor) inhibited GM-CSF-induced conversion of HDN to M-LDN (Fig. 5J, S13C, D). The interaction between

https://doi.org/10.1038/s41467-025-67579-7

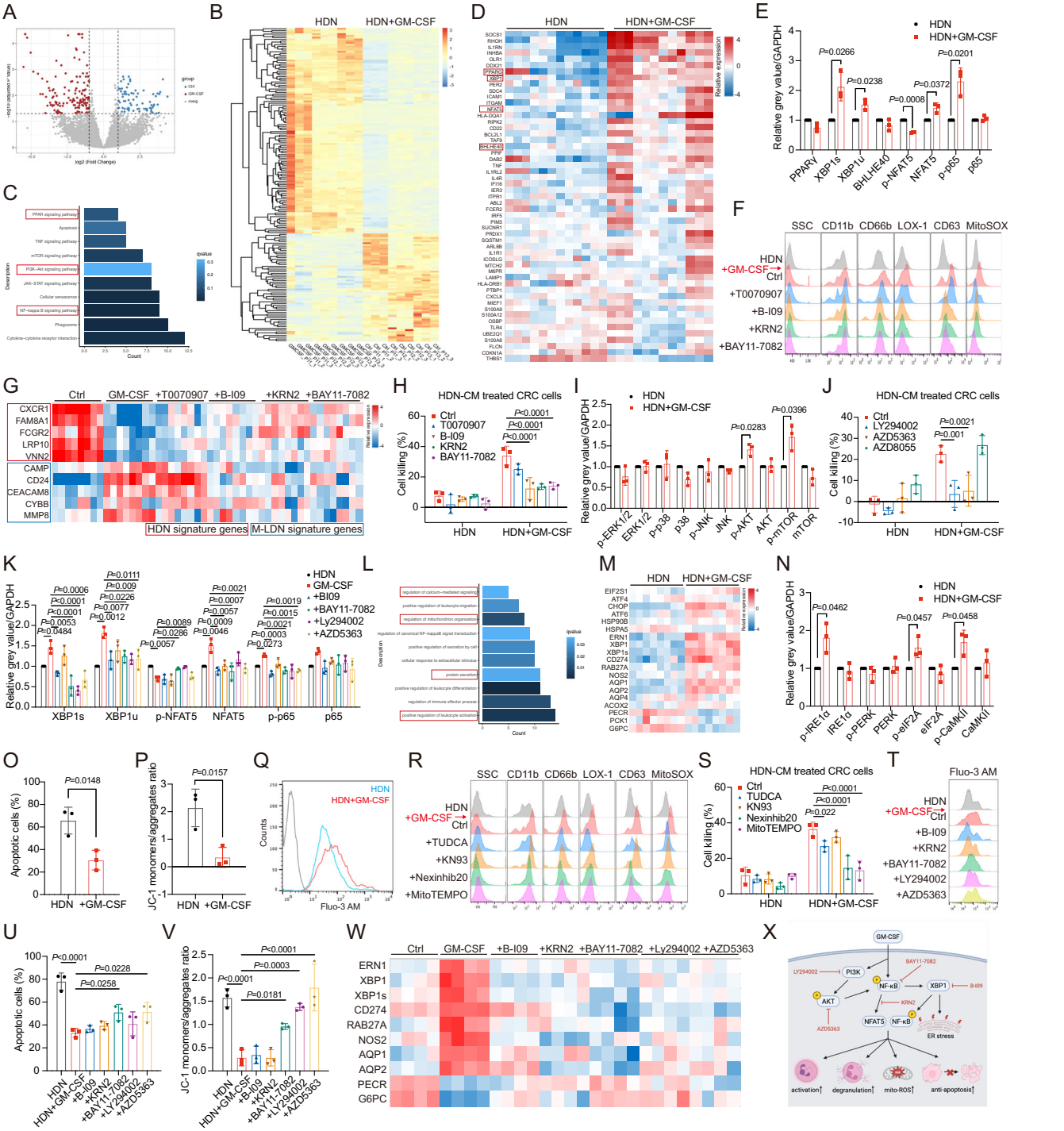

NFAT5 and NF-κB has been reported[50,51]. Western blot confirmed that PI3K/AKT/NF-κB promoted XBP1/NFAT5 expression and participated in the cleavage of XBP1 and dephosphorylation activation of NFAT5, while XBP1/NFAT5 enhanced NF-κB phosphorylation (Fig. 5K, S13E).

GO analysis showed top pathways in GM-CSF-stimulated HDNs including calcium signaling, mitochondrion organization, protein secretion, and leukocyte activation (Fig. 5L). qRT-PCR confirmed GM-CSF upregulated ER stress, immunosuppression, degranulation, water channel, and mitochondrial oxidative stress genes in HDN (Fig. 5M). GM-CSF promoted the activity of ER stress and calcium signaling-related regulatory proteins in HDN (Fig. S13F). GM-CSF inhibited HDN apoptosis (Fig. 5O, S13G), elevated mitochondrial membrane potential (Fig. 5P, S13H), and increased intracellular Ca^{2+} (Fig. 5Q). TUDCA (ER inhibitor), Nexinhib20, and MitoTEMPO pretreatment revealed TUDCA/Nexinhib20/MitoTEMPO blocked the GM-CSF-induced conversion of HDN to M-LDN (Fig. 5R, S).

In vivo, Nexinhib20 decreased the proportion of M-LDNs in the blood of mice, but had no effect on the proportions of HDN or IM-LDN (Fig. S13I). XBP1 and NFAT5 were involved in the regulation of intracellular calcium (Fig. 5T), AKT/ NF-κB was involved in the anti-apoptosis signaling (Fig. 5U, S13J), and PI3K/AKT/NF-κB was involved in the stabilization of mitochondrial membrane potential (Fig. 5V, S13K). qPCR assay showed that NF-κB, NFAT5, PI3K and AKT participated in the regulation of genes related to immunosuppression, degranulation, water channel, and mitochondrial oxidative stress, while XBP1 was mainly involved in the regulation of ER stress (Fig. 5W). The results

Fig. 5 | GM-CSF induces the conversion of HDN to M-LDN through the AKT/NF-κB/NFAT5 axis. DRUG-seq was used to analyze HDNs and HDNs after GM-CSF stimulation. Volcano plot (**A**) and Heatmap (**B**) of differentially expressed genes (DEGs). n = 9, two-sided Wald test. DEGs were defined as |log2FC| > 1 and adjusted p-value < 0.05. **C** KEGG pathway analysis identified top enriched pathways in GM-CSF-stimulated HDNs. **D** qPCR confirmed GM-CSF-induced upregulation of transcription factors *PPARG, XBP1, NFAT5* and *BHLHE40* in HDNs. **E** Western blot showed that GM-CSF upregulated the expression of XBP1 splicing isoform (XBP1s) and NFAT5; promoted phosphorylation of p65; and reduced phosphorylation of p65 NFAT5. n = 3, data were presented as mean ± SD, two-tailed Ratio paired T-test. **F** Inhibitors B-I09 (IRE1 RNase), KRN2 (NFAT5), and BAY11-7082 (NF-κB) blocked GM-CSF-induced conversion of HDN to M-LDN, including the upregulation of CD66b, CD11b, CD63, and LOX-1, as well as the production of mitochondrial ROS. **G** KRN2 and BAY11-7082 blocked GM-CSF-induced conversion of HDN to M-LDN, including downregulated the expression of the HDN signature genes and upregulated M-LDN signature genes. **H** B-I09, KRN2 and BAY11-7082 blocked GM-CSF-induced HDN anti-tumor function. n = 3, data were presented as mean ± SD, two-way ANOVA. **I** Western blot showed that GM-CSF up-regulated the phosphorylation of AKT and mTOR. n = 3, data were presented as mean ± SD, two-tailed Ratio paired T-test. **J** LY294002 (PI3K inhibitor) and AZD5363 (AKT inhibitor) blocked GM-CSF-induced HDN anti-tumor function. n = 3, data were presented as mean ± SD, two-way ANOVA. **K** Western blot demonstrated that GM-CSF upregulated the expression of XBP1s and XBP1u, which could be blocked by B-I09, BAY11-7082, LY294002 and AZD5363; GM-CSF up-regulated the expression of NFAT5, which could be blocked by B-I09, KRN2, BAY11-7082 and AZD5363; GM-CSF up-regulated NFAT5 activation through dephosphorylation, which could be blocked by BAY11-7082 and LY294002; GM-CSF promoted the phosphorylation of p65, which could be blocked by B-I09, BAY11-7082, LY294002 and AZD5363. n = 3, data were presented as mean ± SD, one-way ANOVA. **L** GO pathway analysis shows top enriched pathways in GM-CSF-stimulated HDNs. **M** qPCR confirmed the differentially expressed genes in GM-CSF-induced HDNs associated with endoplasmic reticulum (ER) stress, immunosuppression, degranulation, water channel, and mitochondrial oxidative stress. **N** Western blot showed that GM-CSF upregulated the phosphorylation of IRE1α, eIF2A, and CaMKII in HDNs. n = 3, data were presented as mean ± SD, two-tailed Ratio paired T-test. **O** The apoptosis detection showed that GM-CSF inhibited the apoptosis of HDNs. n = 3, data were presented as mean ± SD, two-tailed unpaired T-test. **P** Mitochondrial membrane potential was determined by JC-1 staining: JC-1 aggregates indicated higher potential; JC-1 monomers indicated lower potential. GM-CSF increased mitochondrial membrane potential in HDNs. n = 3, data were presented as mean ± SD, two-tailed unpaired T-test. **Q** Intracellular Ca^{2+} levels were measured using Fluo-3 AM. GM-CSF increased intracellular Ca^{2+} level in HDNs. **R** TUDCA (ER inhibitor), Nexinhib20 (neutrophil degranulation inhibitor), and MitoTEMPO (mitochondria-targeted antioxidant) blocked the GM-CSF-induced conversion of HDN to M-LDN, including the upregulation of CD66b, CD11b, CD63, and LOX-1, as well as the production of mitochondrial ROS. **S** TUDCA, Nexinhib20, and MitoTEMPO blocked GM-CSF-induced HDN anti-tumor function. n = 3, data were presented as mean ± SD, two-way ANOVA. **T** B-I09 and KRN2 inhibited the GM-CSF-induced increase in intracellular Ca2+ level of HDNs. **U** BAY11-7082 and AZD5363 blocked the anti-apoptosis effect of GM-CSF on HDN. n = 3, data were presented as mean ± SD, one-way ANOVA. **V** The results of JC-1 staining. GM-CSF increased the mitochondrial membrane potential of HDN, which could be blocked by BAY11-7082, LY294002 and AZD5363. n = 3, data were presented as mean ± SD, one-way ANOVA. **W** qPCR results showed that GM-CSF upregulated the expression of ER stress-related genes, which was blocked by B-I09, KRN2, BAY11-7082, LY294002, and AZD5363. GM-CSF upregulated immunosuppression, degranulation, and water channel-associated genes, which was blocked by KRN2, BAY11-7082, LY294002, and AZD5363 GM-CSF downregulated mitochondrial oxidative stress-associated genes, which was blocked by KRN2, BAY11-7082, LY294002, and AZD5363. **X** The mechanism diagram of this chapter. GM-CSF activated the PI3K-AKT pathway in HDN and promoted NF-κB phosphorylation, which was blocked by LY294002 (PI3K inhibitor) and AZD5363 (AKT inhibitor). Additionally, GM-CSF activated NF-κB to induce ER stress via XBP1, which was blocked by BAY11-7082 (NF-κB inhibitor) and B-I09 (XBP1 inhibitor). Moreover, GM-CSF activated NF-κB to promote the expression of NFAT5, and NFAT5/NF-κB synergistically regulated downstream target genes to induce HDN activation, degranulation, mitochondrial ROS production, and anti-apoptosis phenomenon, which was blocked by BAY11-7082 (NF-κB inhibitor) and KRN2 (NFAT5 inhibitor). Created in BioRender. Guo, Z. (2025) https://BioRender.com/8dc71vo. Stimuli concentrations: GM-CSF (10 ng/mL); others as in Supplementary Data. 2. See also Figure S13. Source data are provided as a Source Data file.

suggested that GM-CSF induced the conversion of HDN to M-LDN through phosphorylated activation of PI3K/AKT/NF-κB. Activated NF-κB promoted XBP1 expression (inducing ER stress) and NFAT5 expression, with NFAT5/NF-κB synergistically regulating downstream genes to drive HDN activation, degranulation, mitochondrial ROS production, and anti-apoptosis (Fig. 5X).

CXCR2 ligands activate M-LDN to induce NETosis and promote CRC liver metastasis

Neutrophil subsets from advanced CRC patients showed heightened CXCR2 ligand responsiveness (Fig. 1K). Given that progressive M-LDN increased during tumor progression (Fig. 2), we investigated CXCR2 ligand-specific M-LDN activation. CRC cells potently activated M-LDNs to produce ROS and release H_2O_2 into CM, which was blocked by SB225002 (CXCR2 inhibitors) (Fig. S14A, B). The NETosis induced by CRC cells could also be prevented by SB225002 (Fig. 6A). Among six CXCR2 ligands tested, CXCL5, CXCL6, and CXCL8 induced M-LDN ROS production, H_2O_2 release, and NETosis (Fig. 6B-D).

Numerous studies reported the pro-tumor effects of neutrophils, including their pro-proliferative, anti-apoptotic, and immunosuppressive functions[15,27,29]. Here, CXCL5, CXCL6, and CXCL8 enhanced M-LDN-mediated T-cell proliferation inhibition (Fig. 6E) and cytotoxicity inhibition (Fig. 6F). M-LDNs pretreated with CXCR2 ligands were fractionated into cellular precipitate, NETs, and CM. M-LDN-CM primarily mediated T-cell proliferation inhibition (Fig. 6G), while NETs and CM suppressed T-cell cytotoxicity (Fig. 6H). M-LDNs and NETs suppressed T-cell migration (Fig. 6I, S4C). Immunosuppressive neutrophils inhibit T cell function mainly by releasing ROS, H_2O_2, and ARG1[29,52]. ARG1 secretion analysis revealed CXCR2 ligands activated M-LDNs to secrete ARG1 (Fig. S14D-E). MitoTEMPO, NAC, catalase, and Nor-NOHA (Arg1 inhibitor) were added to M-LDN-CM, and indicated that M-LDN exerted immunosuppressive effects mainly through the release of ROS and H_2O_2 (Fig. 6J, K). NETs reduced CRC cell apoptosis in suspension culture (Fig. 6L, S14F). Immunofluorescence confirmed M-LDNs wrapped CRC cells via NET release (Fig. 6M). CXCR2 ligand-activated M-LDNs promoted CRC proliferation via NETs (Fig. 6N). Public datasets (GSE166555, EMTAB8107, and GSE146771) showed CXCL5, CXCL6, and CXCL8 were expressed in epithelial cells, macrophages, and fibroblasts (Fig. S14G-J), with mIHC confirming CXCL5 and CXCL6 were co-localized with CRC cells, and CXCL8 was co-localized with macrophages (Fig. S14K).

Neutrophils construct pre-metastatic niches by creating immunosuppressive microenvironments and promoting circulating tumor cell colonization[25]. Assessment of neutrophil infiltration in orthotopic CRC mice livers showed significantly increased levels pre-metastasis (Fig. 6O, S15A). Advanced-stage CRC mice exhibited high NETs infiltration (MPO^+citH3^+ regions) and reduced $CD8^+$ T cells in liver tissues (Fig. S15B). CRLM patient tissues confirmed elevated neutrophil and NETs infiltration and diminished $CD8^+$ T cells in paracancer liver (Fig. S15C). Neutrophil recruitment mechanisms revealed CXCL5 co-localized with hepatic stellate cells (FAP^+SMA^+) and hepatocytes (ALB^+), CXCL6 co-localized with HSCs and $CD45^+$ cells, and CXCL8 with $CD45^+$ immune cells (Fig. 6P, S15D). In orthotopic CRC models, colonization of circulating CRC cells in the liver was elevated, and reduced by anti-Ly6G neutrophil depletion or DNase-mediated NET removal (Fig. 6Q). Neutrophil depletion increased $CD8^+$ T-cell infiltration in pre-metastatic livers (Fig. 6R, S15E, F).

IHC staining of liver metastases from patients and mice with CRLM confirmed neutrophil infiltration correlated with higher Ki-67 (proliferation marker), lower TUNEL (apoptosis marker), and reduced

https://doi.org/10.1038/s41467-025-67579-7

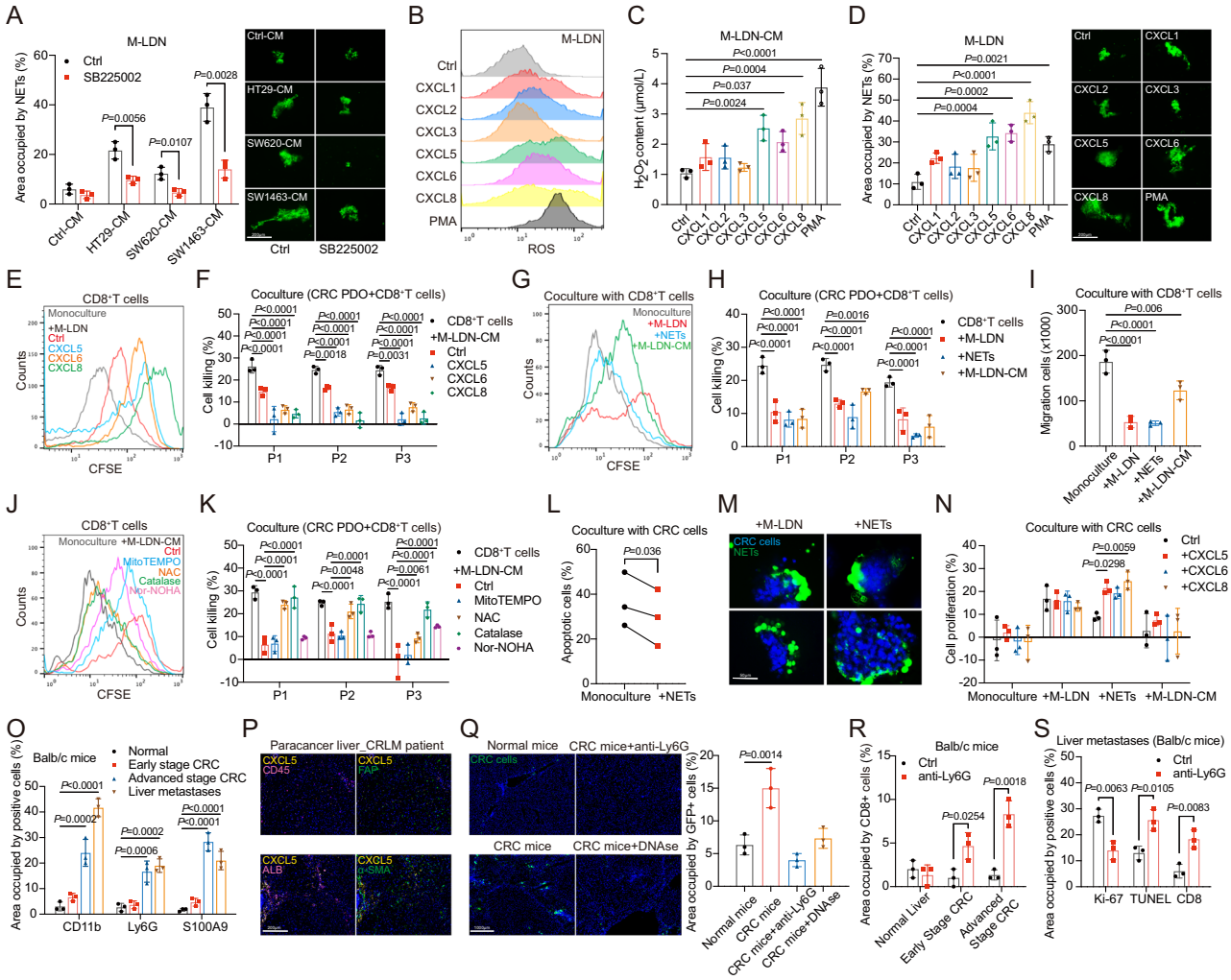

Fig. 6 | CXCR2 ligands activated M-LDN to induce NETosis and promote liver metastasis in colorectal cancer (CRC). A The NETosis assay showed that SB225002 (CXCR2 inhibitors) prevented CRC-induced M-LDN activation. Scale bars, 200 μm. n = 3, data were presented as mean ± SD, two-tailed unpaired T-test. **B** CXCL1, CXCL2, CXCL5, CXCL6, and CXCL8 induced ROS production in M-LDNs. **C** CXCL5, CXCL6, and CXCL8 significantly activated M-LDN to release H_2O_2 into CM. n = 3, data were presented as mean ± SD, one-way ANOVA. **D** CXCL5, CXCL6, and CXCL8 significantly induced M-LDN NETosis. Scale bars, 200 μm. n = 3, data were presented as mean ± SD, one-way ANOVA. **E** CXCL5, CXCL6, and CXCL8 enhanced M-LDN-mediated T-cell proliferation inhibition. **F** CXCL5, CXCL6, and CXCL8 enhanced M-LDN inhibition of $CD8^+$ T-cell-mediated CRC PDO killing. n = 3, data were presented as mean ± SD, two-way ANOVA. **G** M-LDNs were fractionated into three components: cell precipitation, NETs, and CM. M-LDN cells and M-LDN-CM inhibited T cell proliferation. **H** M-LDN cells, NETs, and M-LDN-CM inhibited T-cell-mediated CRC PDO killing. n = 3, data were presented as mean ± SD, two-way ANOVA. **I** M-LDN cells and NETs inhibited T cell migration. n = 3, data were presented as mean ± SD, one-way ANOVA. NAC (ROS scavenger) and catalase prevented M-LDN-mediated inhibition of T-cell proliferation (**J**) and anti-tumor function (**K**). n = 3, data were presented as mean ± SD, two-way ANOVA. **L** NETs reduced the apoptosis of CRC cells under suspension culture. n = 3, data were presented as mean ± SD, two-tailed paired T-test. **M** M-LDNs and NETs wrapped CRC cells in the co-culture environment. Scale bars, 50 μm. **N** CXCL5, CXCL6, and CXCL8 activated M-LDN to promote CRC cells proliferation by releasing NETs. n = 3, data were presented as mean ± SD, two-way ANOVA. **O** The orthotopic CRC spontaneous metastasis model was established via microsurgical Implantation in BALB/c mice. Neutrophil infiltration ($CD11b^+LY6G^+S100A9^+$ cells) in the liver was significantly increased in advanced-stage CRC and metastatic-stage mice. n = 3, data were presented as mean ± SD, one-way ANOVA. **P** mIHC staining showed that CXCL5 primarily co-localized with hepatic stellate cells (HSCs) (FAP^+/SMA^+) and ALB^+ hepatocytes in peritumoral liver tissue of CRC liver metastasis patients. Scale bars, 200 μm. **Q** Compared to normal mice, circulating tumor cell colonization in livers of advanced-stage CRC mice increased but was reduced after anti-Ly6G and DNase treatment. Scale bars, 1000 μm. n = 3, data were presented as mean ± SD, one-way ANOVA. **R** Neutrophil depletion via Ly6G-neutralizing antibodies significantly increased $CD8^+$ T-cell infiltration in the livers of pre-metastatic (early/advanced-stage CRC) mice. n = 3, data were presented as mean ± SD, two-tailed unpaired T-test. **S** Neutrophil depletion significantly inhibited Ki-67 expression while increasing $CD8^+$ T-cell infiltration and $TUNEL^+$ areas in liver metastases. n = 3, data were presented as mean ± SD, two-tailed unpaired T-test. Stimuli concentrations: CXCL5, CXCL6, and CXCL8 (20 ng/mL); others as in Supplementary Data. 2; PMA (25 ng/mL) as positive controls. In Fig. 6 G-M, M-LDNs were pretreated with CXCL5/6/8 mixture (20 ng/mL each). See also Figs. S13-16. Source data are provided as a Source Data file.

$CD8^+$ T cell staining intensities (Fig. S16A, B). Neutrophil depletion via anti-Ly6G decreased Ki-67$^+$ regions but increased $CD8^+$ T cell infiltration and $TUNEL^+$ areas in liver metastases (Fig. 6S, S16C). These results indicate CRC cells activate M-LDNs and induce NETosis via CXCR2 ligands, facilitating liver metastasis by promoting proliferation, anti-apoptosis, immunosuppression, and pre-metastatic niche formation.

CXCR2 ligands induce NETosis in M-LDN through the activation of the MAPK pathway, mediated by NOX and MPO

Key NETosis processes include ROS production, cytoskeleton degradation, and citrolinated histone H3 (cit-H3) formation as previously described[53]. Electron microscopy showed that M-LDN retained cytoplasmic particles, and CXCR2 ligands induced re-degranulation and

https://doi.org/10.1038/s41467-025-67579-7

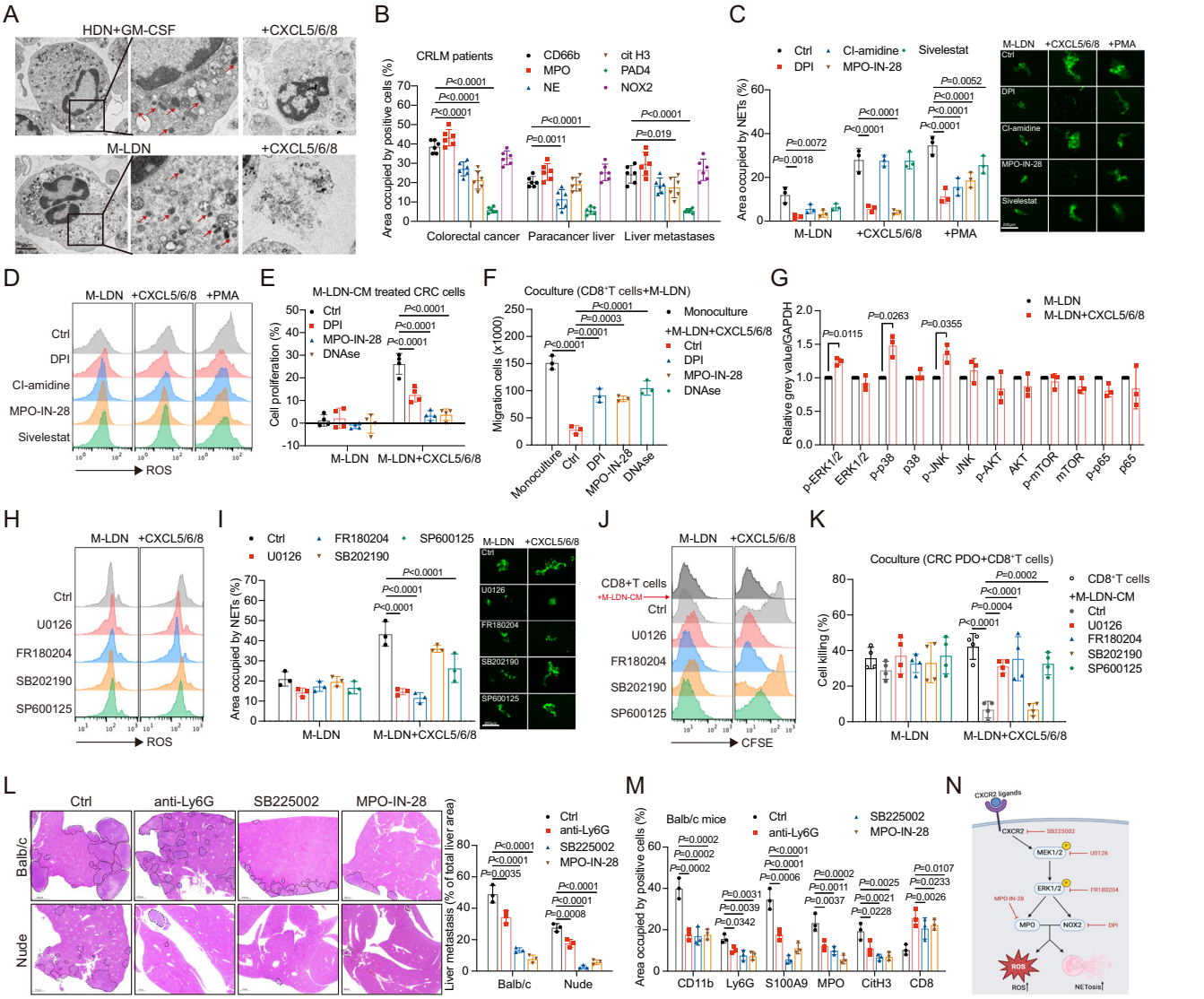

Fig. 7 | The NETosis of M-LDN induced by CXCR2 ligands is dependent on NOX and MPO, via the MAPK pathway. A Electron microscopy shows that the CXCR2 ligands induced re-degranulation and NETosis in M-LDN (derived from CRC patient peripheral blood and GM-CSF-treated HDNs). Data are representative of three independent experiments. Scale bars, 2 μm. **B** Immunohistochemical (IHC) staining of CRC liver metastases confirmed colocalization of $CD66b^+$ neutrophil infiltration with MPO and NOX2 staining in liver metastases and tumor regions. n = 6, data were presented as mean ± SD, two-way ANOVA. **C** The NETosis assay showed that DPI (NADPH oxidase inhibitor) and MPO-in-28 (MPO inhibitor) blocked CXCR2 ligand-induced M-LDN NETosis, whereas DPI, CI-amidine (PAD inhibitor), MPO-IN-28, and sivelestat (NE inhibitor) blocked PMA-induced NETosis. Scale bars, 200 μm. n = 3, data were presented as mean ± SD, two-way ANOVA. **D** DPI and MPO-IN-28 inhibited CXCR2 ligand-induced ROS generation in M-LDNs, whereas DPI, CI-amidine, MPO-IN-28, and sivelestat inhibited PMA-induced ROS generation. **E** DPI and MPO-IN-28 blocked CXCR2 ligand-induced M-LDN promotion of CRC cells proliferation. n = 3, data were presented as mean ± SD, two-way ANOVA. **F** DPI and MPO-IN-28 reversed CXCR2 ligand-enhanced M-LDN inhibition of T-cell migration. n = 3, data were presented as mean ± SD, one-way ANOVA. **G** Western blot analysis showed that CXCR2 ligands upregulated the phosphorylation of ERK1/2 and p38, and JNK. n = 3, data were presented as mean ± SD, two-tailed Ratio paired T-test. **H** U0126 (MEK1/2 inhibitor) and FR180204 (ERK1/2 inhibitor) inhibit CXCR2 ligand-induced ROS generation in M-LDNs. **I** U0126, FR180204, and SP600125 (JNK inhibitor) prevent CXCR2 ligand-induced M-LDN NETosis. n = 3, data were presented as mean ± SD, two-way ANOVA. **J** CXCR2 ligands promoted M-LDN-mediated T-cell proliferation inhibition, which was blocked by U0126, FR180204, and SP600125. **K** CXCR2 ligands promoted M-LDN inhibition of T-cell-mediated CRC PDO killing, which was blocked by U0126, FR180204, and SP600125. n = 3, data were presented as mean ± SD, two-way ANOVA. **L** CT26 was used to establish a liver metastasis model in BALB/c and nude mice. Anti-Ly6G, SB225002 and MPO-IN-28 treatment significantly inhibited liver metastases. Scale bars, 1000 μm. n = 3, data were presented as mean ± SD, one-way ANOVA. **M** Anti-Ly6G, SB225002, and MPO-IN-28 significantly reduced neutrophil infiltration ($CD11b^+LY6G^+S100A9^+$) and NETs (MPO^+citH3^+) but increased $CD8^+$ T-cell infiltration in liver metastases. n = 3, data were presented as mean ± SD, one-way ANOVA. **N** The mechanism diagram of this chapter. CXCR2 ligands (e.g., CXCL5, CXCL6, CXCL8) bind CXCR2 on M-LDNs, activating the downstream MEK1/2-ERK1/2 pathway to induce ROS production and NETosis in an MPO- and NOX2-dependent manner. These processes are blocked by SB225002 (CXCR2 inhibitor), U0126 (MEK1/2 inhibitor), FR180204 (ERK1/2 inhibitor), DPI (NADPH oxidase inhibitor), and MPO-in-28 (MPO inhibitor). Created in BioRender. Guo, Z. (2025) https://BioRender.com/xpwfru8. In Fig. 7, M-LDNs pretreated with CXCL5/6/8 mixture (20 ng/mL each). Stimuli were introduced at the indicated concentration as listed in Supplementary Data. 2. PMA (25 ng/mL) served as positive controls. See also Fig. S17. Source data are provided as a Source Data file.

https://doi.org/10.1038/s41467-025-67579-7

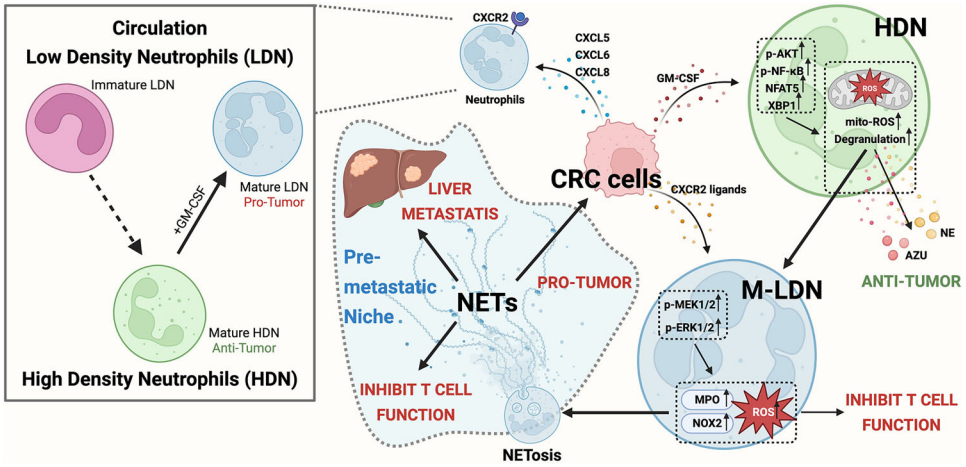

Fig. 8 | Three neutrophil subsets were identified in colorectal cancer (CRC) patients and mice: anti-tumor high-density neutrophils (HDNs), pro-tumor mature low-density neutrophils (M-LDNs), and immature low-density neutrophils (IM-LDNs). CRC cells and liver region secrete CXCR2 ligands (e.g., CXCL5, CXCL6, CXCL8) to recruit neutrophils. CRC cells secreted GM-CSF to induce the degranulation of HDNs into M-LDNs, releasing azurocidin (AZU) and neutrophil elastase (NE) that kill CRC cells via mitochondrial ROS dependent on the AKT/NF-κB/NFAT5 axis. Activated M-LDNs undergo CXCR2 ligand-induced NETosis through NOX/MPO-dependent MEK1/2-ERK1/2 signaling, generating ROS that suppresses T-cell function. NETosis promotes CRC liver metastasis by promoting tumor proliferation, inhibiting apoptosis, inducing immunosuppression, and constructing pre-metastatic niches. Created in BioRender. Guo, Z. (2025) https://BioRender.com/uc7804a.

NETosis in M-LDN (Fig. 7A). Prior studies indicate neutrophil enzymes NE/MPO degrade cytoskeletons while PAD4 induces citH3 formation[54,55]. IHC of CRC liver metastases confirmed colocalization of $CD66b^+$ neutrophil infiltration with MPO and NOX2 staining in liver metastases and tumor regions (Fig. 7B, S17A).

DPI, Cl-amidine (PAD inhibitor), MPO-IN-28, and sivelestat (NE inhibitor) were added during CXCR2 ligand and PMA stimulation of M-LDN. DPI and MPO-IN-28 prevented CXCR2 ligand-induced NETosis and ROS production in M-LDN, while all inhibitors blocked PMA-induced NETosis and ROS production (Fig. 7C, D). Additionally, DPI and MPO-IN-28 abrogated CXCR2 ligand-induced M-LDN promotion of CRC cell proliferation (Fig. 7E) and impaired M-LDN-mediated inhibition of T cell migration (Fig. 7F, S17B).

CXCR2 ligands activated MAPK in M-LDNs (unlike GM-CSF's PI3K-AKT activation in HDNs), MAPK pathway in M-LDN, upregulating phosphorylation of ERK1/2, p38, and JNK (Fig. 7G, S17C). U0126 (MEK1/2 inhibitor), FR180204 (ERK1/2 inhibitor), SB202190 (p38 inhibitor), and SP600125 (JNK inhibitor) were added during CXCR2 ligand stimulation. U0126 and FR180204 prevented CXCR2 ligand-induced ROS production and NETosis in M-LDN (Fig. 7H, I), while U0126, FR180204, and SP600125 blocked CXCR2 ligand-induced M-LDN inhibition of T cell migration and cytotoxic function (Fig. 7J, K).

We evaluated targeting key M-LDN activation mediators as a CRLM treatment strategy. Anti-Ly6G, SB225002 (CXCR2 inhibitor), and MPO-IN-28 inhibited liver metastasis in mice (Fig. 7L, S17D), reducing neutrophil/NETs infiltration while increasing $CD8^+$ T cells in liver metastasis (Fig. 7M, S17E). These treatments decreased blood M-LDNs and NETs (Fig. S17F-I). The results suggested that CXCR2 ligands, such as CXCL5, CXCL6, and CXCL8, bound to CXCR2 on the surface of M-LDN and activated downstream MEK1/2-ERK1/2 pathways to induce NOX/MPO-dependent ROS and NETosis (Fig. 7N).

Clinical significance of the proportion of M-LDN and circulating GM-CSF, CXCR2 ligand, and NETs levels in human and mice with CRC

The relationship between GM-CSF, CXCL5, CXCL6, CXCL8, and NETs levels and the clinical features of the patients with CRC was analyzed. With CRC progression, circulating GM-CSF and CXCL8 initially increased but decreased at stage IV (Fig. S18A, D), while CXCL5, CXCL6, and NETs concentrations progressively increased, peaking in stage IV (Fig. S18B, C, E). Peripheral blood M-LDN proportions positively correlated with circulating GM-CSF, CXCL5, CXCL6, and CXCL8 levels (Fig. S18F-K). Peripheral blood NETs concentrations positively correlated with CXCL5 and CXCL6 levels (Fig. S18L-O). Circulating GM-CSF, LIX (mouse CXCL5), and NETs levels were analyzed in CRC mice. Circulating GM-CSF, LIX, and NETs concentrations increased in advanced-stage CRC and liver metastases (Fig. S18P-R). Peripheral blood M-LDN proportions and NETs concentrations positively correlated with GM-CSF and LIX. NETs concentrations also positively correlated with circulating GM-CSF and LIX levels (Fig. S18S-V).

Discussion

In this study, we investigated the role of CRC cells in promoting liver metastasis through the recruitment and activation of neutrophils. Our results suggest three distinct neutrophil subpopulations in CRC patients and mice models: HDNs may predominantly function as antitumor effectors, M-LDNs appear associated with pro-metastatic characteristics, and IM-LDNs represent an immature state. The CRC cells secrete GM-CSF to activate the AKT/NF-κB/NFAT5 axis and induce the conversion of HDN into M-LDN. This process generates mitochondrial ROS and secreted granulocyte enzymes to kill CRC cells. CRC cells then activate M-LDN by secreting CXCR2 ligands and inducing NETosis, a process that depends on NOX and MPO and is primarily mediated by the MEK1/2-ERK1/2 pathway. During this process, NETosis promotes CRC liver metastasis through pro-proliferation, anti-apoptosis, immunosuppression, and formation of a pre-metastatic niche (Fig. 8).

A previous study suggested that neutrophils play a dual role in malignant tumors; that is, neutrophils can promote tumor growth or prevent tumor progression[16,56]. However, the ability to distinguish between "good" and "bad" neutrophils in cancer is currently limited. Neutrophils can be divided into subtypes such as pro-tumor LDN and anti-tumor HDN[26,32].

Herein, we comprehensively characterized HDNs, M-LDNs, and IM-LDNs through extensive in vitro experiments. HDNs exhibit complete neutrophil functionality, including robust chemotaxis, phagocytosis, tumor-killing capacity, oxidative stress response, degranulation, and NETosis induction, but lack immunosuppressive activity. M-LDNs have impaired chemotaxis and tumor-killing ability but enhanced phagocytosis and oxidative stress response, with

heightened susceptibility to NETosis induction and immunosuppressive function acquisition. IM-LDNs demonstrate defective neutrophil functions and mild immunosuppressive properties. Moreover, we analyzed gene expression profiles of neutrophil subsets in the peripheral blood and tumor tissue of patients with CRC based on DRUG-seq and scRNA-seq analyses. Our neutrophil states showed strong consistency with some published tumor-infiltrating neutrophilic states. Our findings also suggest that HDN, M-LDN, and IM-LDN in the peripheral blood of patients with CRC are highly similar to specific subsets of CRC-infiltrating neutrophils and that HDN and M-LDN have different functions in terms of oxidative burst and T cell activation. Overall, this study contributes evidence that helps differentiate tumor-associated neutrophil subsets, thereby complementing the understanding of their roles in tumors.

Single-cell omics studies have shown that tumor-associated neutrophils (TAN) form a continuous state with different phenotypes[57,58]. Different studies have reported that M-LDNs can be derived from HDN through a TGF-β-dependent mechanism[26,56]. In this study, in vitro observations indicate that M-LDNs could derive from HDNs following GM-CSF stimulation. During this phenotypic transition, HDNs exhibit progressively diminished anti-tumor capacity while acquiring enhanced immunosuppressive activity. Currently, several clinical studies use GM-CSF as an adjuvant in immunotherapy and targeted therapy to enhance anti-tumor responses[59]. In contrast, some researches also emphasized that GM-CSF can recruit MDSCs into tumors to contribute to tumor resistance against VEGFA therapy[60]. Given this contradictory research landscape, our study proposes that when substantial neutrophils infiltrate tumors in response to immunotherapy, GM-CSF may exert anti-tumor effects by enhancing neutrophil cytotoxicity. However, this process could simultaneously drive the generation of M-LDNs and NETs with pro-tumor properties. In our study, M-LDNs, similar to MDSCs, have pro-tumor and immunosuppressive functions. These findings are consistent with those of previous studies on the tumor immune microenvironment, in which immune cells recruited to the TME show anti-tumor effects at the early stages of tumor development, a process known as immune surveillance[61]. However, as the tumor progresses and the inflammatory response continues, immune cells change from immune activators to immune suppressors[62,63].

The role of NETosis in tumor progression and metastasis has recently received considerable attention. Different studies have reported different types of stimulants as initiating factors for NETosis, including immune complexes, complement activators, bacterial peptides, lipopolysaccharides, and chemokines[17,18,27,29]. In this study, we found that CRC cells activate M-LDNs to induce NETosis by secreting multiple CXCR2 ligands in vitro. Similar to previous studies, we have demonstrated the pro-tumorigenic effects of NETs on CRC, including promoting the proliferation of tumor cells, trapping and wrapping circulating tumor cells to resist lost-nest apoptosis, preventing T cell migration, and exerting cytotoxic effects to exert an immunosuppressant function[29,64]. Neutrophils preinfiltrated the premetastatic site, remodeling the pre-metastatic immunosuppressive microenvironment, forming pre-metastatic niches, and increasing tumor colonization by trapping circulating tumor cells through NETs[19,64–67]. Similarly, our study also detected an abnormal accumulation of neutrophils and NETs in the liver before metastasis and demonstrated the role of neutrophils in pre-metastatic niches. These results would facilitate the elucidation of the regulation and functions of NETosis in cancer.

Many studies have been conducted that interfere with the functions of neutrophils using pharmacological methods to inhibit tumor growth and distant metastasis. The in vivo antitumor effects of various therapeutic strategies, including Ly6G neutralizing antibodies, CXCR1/2 inhibitors, DNase I, PAD4 inhibitors, and NE inhibitors, have been reported[18,27–29,64,68]. Our study found that the use of Ly6G neutralizing antibodies to deplete neutrophils in mice, or the use of CXCR2 and MPO inhibitors to block M-LDN activation, inhibited CRC metastasis, whereas an anti-GM-CSF treatment inhibited HDN activation and promoted CRC metastasis. These results support us to develop CRC therapy targeted at M-LDN. Our study found that the use of Ly6G neutralizing antibodies to deplete neutrophils in mice, or the use of CXCR2 and MPO inhibitors to block M-LDN activation, inhibited CRC metastasis, whereas an anti-GM-CSF treatment promoted CRC metastasis. Our work provides evidence deciphering how neutrophil subpopulation transformation and activation regulate CRC liver metastasis, while acknowledging several limitations. Although extensive in vitro experiments utilizing CRC patient-derived primary cells closely modeled parental tumor biology, fundamental differences between in vitro and in vivo environments persist. Consequently, the study lacks robust in vivo models to fully validate the temporal balance between the anti-tumor activity of HDNs and the pro-metastatic function of M-LDNs, particularly considering the potential masking effect of HDN-dominated early responses. While comprehensively characterizing the neutrophil transition from HDN to M-LDN culminating in NETosis, the pursuit of breadth partially compromised mechanistic depth, particularly in genetic-level validation. Furthermore, the proposed mechanisms do not fully account for all experimental observations, especially given the dynamic complexity of the in vivo microenvironment where the net outcome of neutrophil subset activities may shift over time. These gaps underscore the need for future studies employing more complex and extended in vivo models to resolve the context-dependent roles of neutrophil subsets and drive our commitment to further mechanistic investigations to extend the present theoretical framework.

The role of neutrophils in cancer is controversial as they have both pro-tumor and anti-tumor functions. Based on the definition of tumor-associated macrophages, researchers have attempted to distinguish TAN into “N1” types with an antitumor phenotype and “N2” types with a pro-tumor phenotype. However, how the TME affects the polarization of TAN to N1 or N2[56], and whether the polarization of TAN can be artificially manipulated, remain poorly understood[57,63]. Our study reports GM-CSF as the key regulator of HDN-to-M-LDN transformation through activation of the AKT/NF-κB/NFAT5 pathway, alongside CXCR2 ligand-receptor interactions and their downstream MAPK/MPO signaling pathway critical for NETosis induction. The results provide a basis for future research aimed at manipulating TAN polarization by promoting HDN activation (N1 phenotype) and reducing M-LDN activation (N2 phenotype), ultimately inhibiting the progression and metastasis of CRC.

Methods

Ethics approval statement

This study complied with all relevant ethical regulations. All human procedures were reviewed and approved by the Biomedical Ethics Committee of Ruijin Hospital (Approval Nos. 2020-315 and 2021-035) and followed the tenets of the Declaration of Helsinki. All animal experiments were approved by the Laboratory Animal Welfare & Ethics Committee of PHENOTEK Biotech (AUP-220925-01) and conducted in accordance with institutional guidelines.

Patients and specimens

All samples were collected following approval from the Biomedical Ethics Committee of Ruijin Hospital. From 2020–2024, we collected peripheral blood and tumor tissues from patients with colorectal adenoma, CRC, and inflammatory disease at the Ruijin Hospital for research. In addition, we recruited healthy volunteers as controls. All patients with CRC were pathologically diagnosed with CRC and underwent laparoscopic surgery at the Shanghai Minimally Invasive Surgery Medical Center. The exclusion criteria were inflammatory disease, autoimmune disease, infection, neoadjuvant therapy, immunosuppression, or immunomodulatory therapy. TNM staging was

performed in each patient with CRC in accordance with the 2015 National Comprehensive Cancer Network guidelines. All patients were fully informed about the study and had provided written informed consent. For peripheral blood samples, 10 mL of peripheral blood was extracted from each subject using a standard sterilization procedure. The clinical and pathological details of the patients included in this study are provided in Supplementary Data. 1.

Cell lines

Human CRC cell lines SW620 (CCL-227), LOVO (CCL-229), SW480 (CCL-228), SW1463 (CCL-234), HCT116 (CCL-247), Caco-2 (HTB-37), HT29 (HTB-38), DLD1 (CCL-221), RKO (CRL-2577), SW1116 (CCL-233), and SW48 (CCL-231), the mouse colon cancer cell line CT26 (CRL-2638) were purchased from the American Type Culture Collection (ATCC, USA). The normal human colon epithelial cells NCM460 was purchased from INCELL (USA). Human CRC cell lines and NCM460 were cultured in RPMI-1640 medium containing 10% FBS serum and 1% penicillin-streptomycin. CT26 was cultured in DMEM containing 10% FBS and 1% penicillin-streptomycin solution. The primary neutrophils and T cells used in this study were cultured in RPMI-1640 medium containing 10% FBS and 1% penicillin-streptomycin solution. All cells were cultured at 37 °C and 5% CO_2, and cell resuscitation, cryopreservation, passage, and change of CM were performed in strict accordance with aseptic procedures. Cells used in this study were authenticated by STR profiling according to the cell bank.

Lentivirus vectors and shRNA construction

The lentiviral vectors LV3-pGLV-h1-GFP/puro-sh-CXCL5 and LV3-pGLV-h1-GFP/puro-sh-NC were constructed by the Shanghai GenePharma Corporation (China). The sequences of sh-CXCL5 are shown in Supplementary Data. 3. Lentivirus transfection was performed as previously described[7]. The interfering effects of shRNA were evaluated by Western blot and qPCR.

Animal research

All animal procedures in this study were performed at PHENOTEK Biotech (Shanghai) Co., Ltd, which is a commercially accredited animal facility commissioned by Ruijin Hospital. All animal experiments were approved by the Laboratory Animal Welfare & Ethics Committee of PHENOTEK Biotech (AUP-220925-01) and conducted in accordance with institutional guidelines. This study adheres to the ARRIVE (Animal Research: Reporting of In Vivo Experiments) 2.0 guidelines. Animals were euthanized humanely upon achieving predefined experimental endpoints without exceeding the maximum permissible tumor burden (10% of body weight), as stipulated by the Laboratory Animal Welfare & Ethics Committee of PHENOTEK Biotech and the Guide for the Care and Use of Laboratory Animals[69].

Wild-type BALB/c-Nude mice (male, 6-8 weeks old) and BALB/c mice (male, 6-8 weeks old) were purchased from SPF (Suzhou) Biotechnology Co., Ltd. Mice were housed under specific pathogen-free conditions with a standard chow diet, and were maintained at a room temperature of 20–26 °C, a relative humidity of 45–60%, and a 12 h light/12 h dark cycle.

This laboratory investigation evaluated neutrophil dynamics in vivo under conditions mimicking the human colorectal cancer microenvironment. Study endpoints included longitudinal assessment of tumor growth kinetics and comprehensive immunological profiling. Randomization based on tumor volume or baseline measurements was applied in all in vivo experiments to minimize allocation bias. All acquired data meeting predefined inclusion criteria are included in the figures or supplementary materials; no eligible data points were excluded. All values, including statistical outliers within biologically plausible ranges, are reported. Key experiments were independently replicated at least three times using separate biological replicates to ensure robustness and reproducibility.

For the colon cancer in situ model (Fig. S4A-C, S4E, S4G, S4I-J), mice were anesthetized by intraperitoneal injection of 1% pentobarbital sodium. A left mid-abdominal incision was made to expose the cecum, and 1×10^7 tumor cells suspended in 100 µL PBS were slowly injected into the cecal wall. The cecum was repositioned within the abdominal cavity, and the abdomen was closed. Four weeks post-implantation, mice were euthanized. Tumor burden was quantitatively assessed using two approaches: (1) excised cecal tumors were weighed to determine fresh tissue mass; (2) hematoxylin and eosin (H&E)-stained sections were analyzed to calculate the percentage of total cecum area occupied by tumor tissue.

For the liver metastasis model (Figs. 1A-C, 3T, 4O, 6S, 7L, M, and Figs. S4D, S4F, S4H, S9E-F, S12C-E, S16A, S16C, S17D-I), mice were anesthetized by intraperitoneal injection of 1% pentobarbital sodium. Following abdominal incision, the spleen was exteriorized, and 1×10^7 tumor cells suspended in 100 µL PBS were slowly injected into the splenic parenchyma. The spleen was repositioned into the abdominal cavity, and the incision was sutured. Four weeks post-injection, mice were euthanized. Liver metastasis burden was quantified by calculating the percentage of tumor area occupancy relative to total liver area in H&E-stained sections.

For the subcutaneous xenograft model (Fig. S12F-I), mice were anesthetized via intraperitoneal injection of 1% pentobarbital sodium. A suspension containing 1×10^7 tumor cells in 100 µL PBS was injected into the subcutaneous space of the mid-dorsal region. Tumor growth was monitored twice weekly by caliper measurements (volume = length × width^2 × 0.5) until endpoint. Four weeks post-injection, mice were euthanized, subcutaneous tumors were surgically excised, and fresh tissue mass was immediately quantified using an analytical balance.

For neutrophil depletion studies (Figs. 1C, 6R, S, S15E, F, S16C), mice received intraperitoneal injections of 200 µg anti-Ly6G antibody (Clone 1A8) or rat IgG isotype control every 3 days post-tumor inoculation. Primary human neutrophils were isolated from CRC patient peripheral blood via Histopaque®–1077/1119 gradient centrifugation. For adoptive transfer, 5×10^6 neutrophils were delivered by: (1) tail vein injection in liver metastasis models for systemic distribution (Fig. 3T, S9E, F), or (2) multi-point intratumoral injection at three sites surrounding the tumor periphery in subcutaneous tumor models (Fig. S12F-G). Subsequent transfers occurred every 3 days, preceded by 1A8-mediated depletion 24 h prior to each transfer.

The orthotopic CRC model with spontaneous metastasis was established using Microsurgical Implantation (MSOI)[33] (Fig. S6B). Briefly, CT26 cells (2×10^7 cells in 100 µL PBS) were subcutaneously inoculated into the right flank of BALB/c mice. After palpable tumors formed, tumor tissues were surgically excised, minced into 1-mm^3 fragments, and sutured onto the serosal surface of the cecum through a midline laparotomy. Tumor progression was longitudinally monitored: Visible cecal tumors developed by day 7 post-implantation (early-stage CRC), exhibited rapid growth without hepatic metastasis by day 14 (advanced-stage CRC), and demonstrated spontaneous liver metastases by day 21 (metastatic-stage). Peripheral blood samples were collected at these timepoints (days 7, 14, 21) (Fig. 2J, S18P-V). Following euthanasia and necropsy, primary tumor burden (cecal mass) and metastatic dissemination were quantified, and tissues were harvested as required (Figs. 2O, P, 6O, R, Fig. S15A, B, S15E, F).

For the colonization assays (Fig. 6Q), orthotopic colorectal tumors were established in BALB/c mice via MSOI of CT26 fragments. Mice were stratified into three pre-conditioning cohorts receiving intraperitoneal injections of: (1) 1A8 Ly6G antibody (200 µg/mouse) every 3 days until splenic injection; (2) DNase I (5 mg/kg) for 3 consecutive days prior to splenic injection; (3) PBS vehicle control. Fourteen days post-MSOI, 2×10^5 GFP-expressing CT26 cells in 100 µL PBS were injected into the splenic parenchyma. Mice were euthanized 36 h

post-injection, and colonization was assessed by immunofluorescence imaging of liver sections.

For the inflammation model (Fig. S10F-J), mice were intraperitoneally injected with PBS control or LPS (2.5 mg/kg), and after 24 h, peripheral blood samples were collected and used for further analyses.

Beginning on day 7 post-tumor cell injection, mice received intraperitoneal injections every 3 days until the 4-week endpoint with: (1) anti-Ly6G (1A8, 200 μg/mouse), anti-GM-CSF (200 μg/mouse), or rat IgG isotype control (Figs. 4O, 7L-M, S12C-E, S12H-I, S17D-I); (2) small-molecule inhibitors SB225002 (CXCR2 antagonist, 5 mg/kg) or MPO-IN-28 (myeloperoxidase inhibitor, 5 mg/kg), with DMSO vehicle control (Fig. 7L, M, S17D-I); (3) recombinant mouse GM-CSF (200 ng/mouse) with PBS vehicle control (Fig. S12H-I).

Peripheral blood was collected via terminal cardiac puncture under anesthesia, followed by isolation of high-density neutrophils (HDNs), low-density neutrophils (LDNs), and serum using Histopaque® −1077/1119 density gradient centrifugation. Post-euthanasia, tissues were harvested as required: tumor-bearing and non-tumor-bearing liver lobes, tumor-adjacent and normal colonic segments, and subcutaneous tumors. Samples underwent snap-freezing in liquid nitrogen, fixation in 4% paraformaldehyde (24 h for paraffin embedding), or OCT embedding for cryosectioning. Serial 5-μm sections were prepared for H&E staining and immunohistochemistry (IHC). Reagents used for animal experiments are listed in Supplementary Data. 2.

Bioinformatics analysis

The expression levels of neutrophil markers, CXC chemokines,and *CXCR2* in CRC were analyzed using the UALCAN and GEPIA databases. Neutrophil infiltration into the tumor was analyzed using the TIMER database (http://timer.cistrome.org). The mutation information and gene expression of CRC cell lines were obtained from the CCLE and DepMap (https://depmap.org/) databases.

DRUG-seq

Total RNA was extracted using TRIzol reagent and purified by using the phenol-chloroform method. Total RNA was mixed and incubated with Drug beads and 2× Binding Buffer to capture Poly(A) RNA. DTT, dNTP, RNase inhibitor, and RT enzyme, and 5× RT Buffer was added to the previous product to synthesize a strand cDNA. Single-stranded DNA was removed by adding Exonuclease I and 10× Exonuclease I Buffer, and the Poly(A) RNA was removed by adding Elution Buffer. Random primer, 10× Reaction Buffer, enhancer, dNTP, and cDNA Extend Polymerase I were used for the two-strand cDNA synthesis. DNA beads were added to the supernatant for fragment recovery. Next, 2× HIFI Amplification Mix and index were added, followed by PCR Amplification for library fragments. DNA beads were screened for library fragments. Bioptic Qsep100 Analyzer was used for library quality inspection to check whether the library size distribution is in line with the theoretical size. NovaSeq high-throughput sequencing platform and PE150 sequencing mode were used for sequencing. DRUG-seq was performed by Guangzhou Epibiotek Co., Ltd. on an Illumina NovaSeq 6000 platform (Illumina, San Diego, CA, USA)[70]. Raw reads were filtered to remove the adapter by cutadapt (v2.5; https://cutadapt.readthedocs.io/en/stable/). The sequenced reads were single-end mapped to reference genome sequences (GRCh38) using NextGenMap (v0.5.5; http://cibiv.github.io/NextGenMap/) and SAMtools (v1.10; http://samtools.sourceforge.net). We used featureCounts (v1.6.3; https://subread.sourceforge.net/featureCounts.html) to perform quantification on the mapped sequences. The differential expression analysis was performed with the DESeq2 (v1.18.1), and differentially expressed genes (DEGs) are defined as those with FoldChange > 2 and p value < 0.05. KEGG and GO enrichment analysis was performed using the package clusterProfiler (v4.10.1) and visualized by pheatmap (v1.0.12).

Comparison with published scRNA-seq data for human neutrophils

Published scRNA-seq data of human neutrophils were downloaded[36–40]. To compare the expression similarity of clusters, we chose the highly variable genes and calculated Spearman rank correlation. To compare the expression similarity of clusters, we chose the highly variable genes and calculated Spearman rank correlation. The gene lists of different neutrophil subtypes were generated from https://github.com/wu-yc/neutrophil[71] (PRJCA020880) and the scores of HDN, IM-LDN and M-LDN were calculated using the GSVA package (v1.50.0).

scRNA sequencing

CRC samples were taken from patients during surgical debulking. The clinical characteristics of the collected tumor samples are summarized in Supplementary Data. 1. scRNA-seq was performed with GEXSCOPE Single Cell RNA Library kits (Singleron)[72]. All steps were performed following the standard manufacturer protocols. The concentrations of single-cell suspensions were adjusted to target a recovery of 7,000–10,000 cells per sample. The libraries were sequenced on an Illumina HiSeq X Ten sequencer. The reads were mapped to the GRCh38 genome using STAR and gene counts, and unique molecular identifier counts were generated with 'featureCounts' software. After quality control, we used the standard analysis pipeline of the R package Seurat (v5.0.1)[73]. We used the 'FindMarkers' function of Seurat with default parameters to identify DEGs. The genes expressed in at least 25% of cells in a cluster of interest were selected and further filtered using a minimum log2 (fold change) of 0.5 and a maximum false discovery rate of 0.01. The Python package scEntropy (https://github.com/jzlei/scEntropy) was used for the calculation. To visualize the likelihood of cell entropy, we constructed the entropy landscape by integrating the dimensional reduction representation of scRNA-seq data and the cellular entropy estimation for each cell. RNA velocity analyses were used to infer cell trajectories[74]. The Python package Velocyto was used to determine the unspliced/spliced/ambiguous transcripts and scVelo was used to calculate the RNA velocity of neutropuils. The velocity (moments) of spliced/unspliced counts was calculated using the functions 'scv.pp. moments' and 'scv.tl. velocity' with the mode set to 'dynamical'. Gene set enrichment analysis was performed using the highly expressed genes. We used Gene Ontology (GO) to quantify the pathway activity of neutrophils[75]. Ucell (v2.7.5) was used to calculated different neutrophil scores for HDN, IM-LDN, and M-LDN.

Immunohistochemical (IHC) analysis

Tissues were fixed in 4% neutral-buffered formalin, embedded in paraffin, and cut into 7-μm sections. A tissue microarray, including 78 pairs of CRC samples, as described in our previous study[7,76], was used for immunohistochemical (IHC) staining. IHC staining was performed according to the manufacturer's protocol (Immunostain SP Kit; Dako Cytomation, USA). The antibodies used for IHC analysis are listed in Supplementary Data. 1. IHC staining was scored semi quantitatively by two independent pathologists.

Peripheral blood neutrophil extraction

Whole blood neutrophils were enriched using the MACSxpress® Neutrophil Isolation Kit, according to the manufacturer's protocol. The freeze-dried antibody powder and buffer were pre-mixed and then added to the anticoagulated blood at a volume ratio of 8 mL anticoagulated whole blood and 4 mL of the separation solution. The antibody was incubated for 5 min, and the tube was placed in the magnetic field of the magnetic pole for 15 min. The cells labeled by the magnetic beads adhered to the wall of the tube, and the supernatant components were collected. The supernatant containing the target cells was

centrifuged at 20 °C (300 × *g*) for 10 min. Red blood cells were eliminated through hypotonic lysis using red blood cell lysis buffer.

Cell medium (CM) preparation

The cells were cultured in RPMI-1640 medium containing 10% FBS and 1% penicillin–streptomycin solution. Once the adherent cells reached 100% confluence, the cell CM was replaced with fresh medium. For the cell suspension, and 1×10^7 cells were cultured in 1 mL of fresh medium. The cell CM was collected after 24 h.

Cell migration assay

The procedure of cell migration assay was as previously described[17]. A transwell chamber (5 μm for 24-well plates, Corning Costar) was used to perform the cell migration assay. Serum-free medium (200 μL) containing 1×10^5 neutrophils was added into the upper transwell chamber, whereas 800 μL of the CRC cell CM or complete medium was added into the lower chamber, and recombinant proteins or inhibitors were added based on the group. After incubation for 4 h, the number of cells in the lower chamber was counted. For the NET migration assay, 100 μL of serum-free medium containing 2×10^5 neutrophils or NETs was added into the upper transwell chamber, and recombinant proteins or inhibitors were added as required by the experiment. Next, 100 μL of serum-free medium containing 2×10^5 GFP-labeled T cells was added to the upper transwell chamber, and 800 μL complete medium containing CCL5 was added into the lower chamber. After 4 h of incubation, the GFP-labeled cells in the lower chamber were counted.

NETosis analysis

Prior to NETosis detection, the neutrophils were pre-treated with CRC cell CM, recombinant proteins, and inhibitors according to the group for 4 h. Extracellular neutrophils were monitored using a cell-impermeable nucleic acid stain (SYTOX Green, 5 μM), followed by incubation at 20 °C for 10 min in the dark. Images were captured and analyzed using fluorescence microscopy.

Separation of high-density layer cells and low-density layer cells

For peripheral blood samples, heparinized blood (20 U/mL) was mixed with an equal volume of phosphate-buffered saline (PBS) and carefully layered onto a discontinuous Histopaque (Sigma) gradient (1.077 and 1.119). For tissue samples, the tumor tissue was washed with PBS containing penicillin-streptomycin solution. The tissues were then chopped, added to DMEM containing 3 mg/mL collagenase IV (Sigma) and 5 MU/mL DNase I (Sigma), followed by digestion at 37 °C for 30 min. The digested tissue suspension was passed through a 100-μm filter to remove residual tissue. The filtrate was then collected and centrifuged to precipitate the cells. The cell precipitates were re-suspended in PBS and carefully stratified using a density gradient centrifuge. For spleen samples, the spleen was ground to release cellular components. The cell precipitates were suspended in PBS and carefully stratified using a density gradient centrifuge. The density gradient consists of Histopaque-1077 human lymphocyte isolation solution (Sigma-Aldrich) in the upper layer and Histopaque-1119 density gradient isolation solution (Sigma-Aldrich) in the lower layer. The cells were centrifuged at 220 × *g* for 20 min at 20 °C. High-density cells were collected from the 1.077–1.119 interface and low-density cells were collected from the red plasma-1.077 interface. Red blood cell lysis buffer was used to eliminate red blood cells, followed by the addition of 10 mL of 1.6% NaCl to restore the isotonic properties. Finally, the neutrophils were washed thrice with PBS.

Hematoxylin staining of neutrophils

Neutrophils were prepared by cell smear centrifugation at 20 °C (300 × *g*) for 10 min, fixed with 4% paraformaldehyde for 20 min, and washed several times with distilled water for 2 min per time. The sections were stained with a hematoxylin staining solution for 5–10 min, rinsed with tap water for approximately 10 min to remove excess staining solution, and washed again with distilled water. The results were visualized under a microscope.

Flow cytometry analysis

Neutrophils were centrifuged at 20 °C (300 × *g*) for 10 min, washed with staining buffer (PBS containing 3% FBS) and collected into the flow tube at a concentration of 10^6 cells per 100 μL. Fluorescent-conjugated primary antibodies were used to stain cells at 4 °C in the dark for 30 min. Antibodies against CD11b, CD14, CD66b, CD16, CD45, CD15, LOX-1, CD63, CD54, CD274, CD10, CXCR2, and Ly6G were used. The samples were subjected to flow cytometry (BD Biosciences), followed by analysis with FlowJo software (Tree Star). Additional information on the antibodies is listed in Supplementary Data. 2.

Magnetic-activated cell sorting

Cells were fully suspended in magnetic-activated cell sorting (MACS) incubation solution (1×10^8 cells/0.5 mL). Primary antibody was added (20 μg/mL), followed by incubation at 4 °C for 30 min. Primary antibodies against CD11b, CD66b, CD14, CD3, and CD8 were used. The MACS incubation solution was used to clean the cells. The MACS incubation solution (1×10^8 cells/0.2 mL) was added to fully suspend the cells. Magnetic beads coated with corresponding secondary antibodies were added, and the mixture was incubated at 8 °C for 15 min. The separation column was installed in the magnetic pole, and 0.5 mL of MACS incubation solution was added to pretreat the separation column. The cell suspension was added to the separation column and allowed to drain. After the MACS incubation solution was washed off, the separation column was removed for elution and the target cells collected. Additional information on the antibodies is listed in Supplementary Data. 2.

Phagocytosis assay

Neutrophil phagocytic activity was measured using a Phagocytosis Assay Kit (Cayman Chemistry) according to the manufacturer's instructions. Briefly, 1×10^6 neutrophils were reinserted in 200 μL of phagocytosis buffer, followed by the addition of FITC-labeled microspheres (1:100) and incubation at 37 °C for 2 h. The degree of phagocytosis was measured by using fluorescence microscopy or flow cytometry (BD Biosciences).

Killing and proliferation assays

CRC or non-cancer cells were inoculated into 96-well plates at a concentration of 2×10^3 cells/well and grown to 70–80% confluence. Purified neutrophils were added to adherent cells at a concentration of 10×10^3 cells/pore and co-cultured overnight. The wells were washed twice with PBS, and next, 10 μL CCK-8 (APExBIO, USA) and 90 μL complete media were added to each well prior to testing. The mixture was incubated at 37 °C for 2 h, and the OD values were determined using a spectrophotometer (BioTek, Winooski, USA).

Cell co-culture

Transwell chambers (0.4 μm for 24-well plates, Corning Costar) were used for co-culture. Complete medium (200 μL) containing 1×10^5 purified neutrophils was added to the upper transwell chamber, whereas 800 μL of complete medium containing 1×10^5 CRC cells or non-cancer cells was added to the lower chamber and co-cultured overnight. The two cell types were cultured separately, but with the same cell medium. The cells were cultured in RPMI-1640 with 10% FBS and 1% penicillin-streptomycin at 37 °C and 5% CO_2.

Apoptosis detection

Flow cytometry assay to assess apoptosis was performed as previously described[77]. The Annexin V-FITC Apoptosis Detection Kit (BD

Pharmingen, USA) was used to detect cell surface Annexin V expression and propidium iodide (PI) uptake using flow cytometry according to the manufacturer's instructions. The cells were collected, washed twice with ice-cold PBS, and suspended in 100 μL binding buffer. Annexin V-FITC (3 μL) and PI (5 μL) were used to stain the cells in the dark at 20 °C for 15 min. Apoptosis was analyzed by flow cytometry using a FACSCalibur system (BD Biosciences).

Peripheral blood T cell extraction

The MACSprep™ HLA Cell Isolation Kit was used to enrich T cells in whole blood according to the manufacturer's protocol. MACSprep HLA cell isolation solution was added to the anticoagulant, rotated, and incubated for 5 min. The tube was placed in the magnetic field of the magnetic pole for 15 min, where the cells labeled with magnetic beads adhered to the wall of the tube, and the supernatant components were collected. The supernatant containing the target cells was centrifuged at 20 °C (300 × *g*) for 10 min. Red blood cell lysate was added to the precipitate, and T cells were obtained after removing the red blood cells. Magnetic bead sorting was performed using CD3 or CD8 to further purify the T cells.

T cell labeling and proliferation in vitro

T cells were obtained from the peripheral blood of patients with CRC. The cells were re-suspended at 1×10^7 cells/mL in pre-warmed PBS containing CSFE (1 μM, Invitrogen) and incubated at 37 °C for 10 min. Labeling was quenched by adding CM containing 10% FBS and washing twice with PBS. T cells were inoculated into RPMI 1640 medium containing 20 IU/mL IL-2 at a density of 2×10^6 cells/mL and stimulated with anti-CD3/CD28 antibodies. Purified neutrophils were cocultured with T cells according to the experimental design. After 72 h of culture, the CFSE levels were detected using flow cytometry.

Patient-derived organoids (PDOs) culture

CRC PDOs were embedded in Matrigel (BD, USA) and overlaid with organoid culture medium, including 50 ng/mL EGF (PeproTech, USA), 500 nM A83-01 (AbMole, USA), 50 ng/mL Noggin (PeproTech, USA), 3 μM SB202190 (AbMole, USA), 10 nM prostaglandin E2 (AbMole, USA), and 1X B27 (Gibco, USA). TrypLE™ Express Enzyme (Thermo Scientific, USA) was used to digest the Matrigel to release PDOs[77].

T cell cytotoxicity assays

For cytotoxicity assays[78], CD8 T cells were pre-stimulated with 20 IU/mL IL-2 and anti-CD3/CD28 antibodies for 48 h. As required, T cells were co-cultured with neutrophils at this step. 5 × 103 luciferase-labeled organoids cells were seeded per well of the 96-well plate, and were grown for 24 h before addition of T cells. CD8 T cells were added to PDOs at a concentration of 10^4 cells/pore and co-cultured for 48 h. For luciferase-based quantification, the supernatant was removed after co-culture and each well was washed with pre-warmed culture medium. Subsequently, 500 μl luciferase assay reagent composed of 10% One-Glo EX Reagent (Promega) in lysis buffer was added to each well and incubated at room temperature for 15 min protected from light. Lysates were measured using FlexStation. Cell killing ratio was defined as the difference between luciferase activity of organoids cultured alone and residual luciferase activity after co-culture.

H_2O_2 measurements

Purified neutrophils were activated with PMA (25 ng/mL), ionomycin (5 μM), LPS (100 ng/mL), and fMLP (0.5 nM) to induce the generation of H_2O_2. Measurements were performed using a hydrogen peroxide assay kit (S0038, Beyotime Biotechnology) according to the manufacturer's instructions.

ROS detection

Dihydroethidium and MitoSOX were used to detect cytosolic and mitochondrial ROS, respectively. The purified neutrophils were activated with PMA (25 ng/mL), ionomycin (5 μM), LPS (100 ng/mL), and fMLP (0.5 nM) for 1 h. Flow cytometry was used for quantitative analysis.

Enzyme-linked immunosorbent assay

The cell CM was collected from CRC and non-tumor cells. Cytokine levels were measured using the Human Neutrophil Elastase enzyme-linked immunosorbent assay (ELISA) Kit (RayBiotech), Human Myeloperoxidase/MPO ELISA Kit (RayBiotech), Human Azurocidin/CAP37/HBP ELISA Kit (RayBiotech), Human Cathepsin G ELISA Kit (Abcam), Human IL-8/CXCL8 ELISA Kit (Abclonal), and Human CXCL5/ENA-78 ELISA Kit (abclonal), Human GM-CSF ELISA Kit (abclonal), Human IFN-gamma ELISA Kit (abclonal), and Human ARG1 ELISA Kit (abclonal), all according to the manufacturer's instructions.

Electron microscopy

The neutrophils were immediately fixed in 2% glutaraldehyde and 2% paraformaldehyde in 0.1 mol/L sodium phosphate buffer (pH 7.4) at 4 °C for 3 h. The fixed cells were then embedded, sectioned and stained with osmium tetroxide and uranyl acetate. Sections were examined on a Hitachi electron microscope equipped with a digital camera.

RNA extraction and qRT-PCR

The procedure of the RNA extraction and qRT-PCR analysis was previously described[76]. Total RNA was extracted from purified neutrophils using the TRIzol reagent (Invitrogen, Carlsbad, CA, USA) according to the manufacturer's instructions. The RNA concentration was measured using a Nanodrop 2000 (Thermo Scientific, USA). Total RNA was reverse transcribed to cDNA using HiScript III RT SuperMix (Vazyme), and qPCR was performed using SYBR Green (Vazyme) according to the manufacturer's instructions. The primers for qPCR were purchased from Genewiz (China), and the sequences are listed in Supplementary Data. 4. GAPDH was used as the control. The relative expression ratio of mRNAs in each group was calculated using the $2^{-\Delta\Delta CT}$ method.

Neutrophil isolation

Neutrophils were pre-treated with the recombinant protein and PMA for 4 h. Neutrophils were collected, centrifuged at 480 × *g* for 10 min, and precipitated as cellular components. The supernatant was then centrifuged at 18,000 × *g* for 15 min and the NETs components precipitated.

Centrifugal filtration

Centrifugal filtration was performed using an Amicon Ultra centrifugal filter unit (Millipore), according to the manufacturer's instructions. The pore sizes of the selected membranes were 100 kDa, 30 kDa, and 10 kDa. In brief, approximately 500 μL cell medium was added to the filter and centrifuged at 14,000 × *g* for 15 min. The filter was then reversed and centrifuged at 2,000 × *g* for 5 min to collect the purified CM.

Luminex assay

Cytokine levels were measured using a Luminex X-MAP system (Luminex 200 system, Luminex Corporation, Austin, TX, USA) and a Bio-Plex Pro Human Chemokine Panel 40-plex (Bio-Rad Laboratories, California, USA). The assay was performed according to the manufacturer's instructions (Wayen Biotechnologies)[79]. The Bio-Plex Pro Human Chemokine Panel 40-plex allows for the simultaneous detection of the following circulating analytes: 6Ckine/CCL21, BCA-1/CXCL13, CTACK/CCL27, ENA-78/CXCL5, Eotaxin-2/CCL24, Eotaxin-3/CCL26, Eotaxin/CCL11, Fractalkine/CX3CL1, GCP-2/CXCL6, GM-CSF, Gro-α/CXCL1, Gro-β/CXCL2, I-309/CCL1, I-TAC/CXCL11, IFN-γ, IL-10, IL-

16, IL-1β, IL-2, IL-4, IL-6, IL-8/CXCL8, IP-10/CXCL10, MCP-1/CCL2, MCP-2/CCL8, MCP-3/CCL7, MCP-4/CCL13, MDC/CCL22, MIF, MIG/CXCL9, MIP-1α/CCL3, MIP-1δ/CCL15, MIP-3α/CCL20, MIP-3b/CCL19, MPIF-1/CCL23, SCYB16/CXCL16, SDF-1α + β/CXCL12, TARC/CCL17, TECK/CCL25, and TNF-α. Concentrated human recombinant standards were provided by the vendor, and a broad range of standards were used to establish standard curves. The samples and standards tested in this experiment were detected using a Luminex 200 detector, and the obtained fluorescence was automatically calculated and optimized using the software. The original fluorescence of each sample was substituted into the standard curve to calculate the sample concentration. The cytokine concentrations are provided in Supplementary Data 6.

Cytokine microarray analysis

Cytokine levels were measured using a RayBio Human Cytokine Antibody Array G-Series 6 kit (AAH-CYT-G6-4, RayBiotech) according to manufacturer's instructions. The Human Cytokine Antibody Array G-Series 6 kit allows for the simultaneous detection of the following cytokines: BDNF, BLC, BMP-4, BMP-6, CK beta 8-1, CNTF, EGF, eotaxin, eotaxin-2, eotaxin-3, FGF-6, FGF-7, Flt-3 ligand, fractalkine, GCP-2, GDNF, GM-CSF, I-309, IFN-γ, IGFBP-1, IGFBP-2, IGFBP-4, IGF-I, IL-10, IL-13, IL-15, IL-16, IL-1α, IL-1β, IL-1ra, IL-2, IL-3, IL-4, IL-5, IL-6, IL-7, leptin, LIGHT, MCP-1, MCP-2, MCP-3, MCP-4, M-CSF, MDC, MIG, MIP-1-δ, MIP-3-α, NAP-2, NT-3, PARC, PDGF-BB, RANTES, SCF, SDF-1, TARC, TGFβ−1, TGFβ−3, TNF-α, and TNF-β. The cytokine concentrations are provided in Supplementary Data 7.

Tumor spheroid formation

The HT29 CRC cells were inoculated into a non-adherent culture plate to form tumor spheroids, as previously described[80]. HT29 tumor spheroids were co-cultured with neutrophils and NETs for 24 h. Extracellular NETs were stained with SYTOX Green (5 μM) and incubated at 20 °C in the dark for 10 min. Images were captured and recorded using a fluorescence microscope.

Protein extraction and western blotting

Protein extraction and western blotting were performed as previously described[7]. Neutrophils were collected by centrifugation, and total protein was extracted using RIPA buffer (Solarbio, China) in the presence of a Protease Inhibitor and Protein Phosphatase Inhibitor Cocktail (APExBIO, USA). The total protein concentration of the lysate was quantified using a BCA Protein Assay Kit (Thermo Fisher Scientific, Waltham, MA, USA). Proteins were separated using sodium dodecyl sulfate-polyacrylamide gel electrophoresis (SDS-PAGE) and transferred onto a PVDF membrane (Tanon, China). The membranes were blocked with 3% bovine serum albumin (BSA) for 2 h and incubated with primary antibodies at 4 °C overnight. Goat anti-rabbit or goat anti-mouse horseradish peroxidase-conjugated IgG (H + L) was used as a secondary antibody, and the samples were incubated at 37 °C for 2 h. An ECL chemiluminescence agent (Millipore, USA) was used to visualize the membranes, and images were captured using a Tanon Chemiluminescence Imaging System (Tanon, China). GAPDH was used as an internal control. Additional information on the antibodies is listed in Supplementary Data 2.

BioRender statement

Some figures were created using BioRender.com. Publication licenses were secured in compliance with BioRender's academic licensing terms. Attribution is provided in relevant figure legends per BioRender's citation requirements.

Quantitative and statistical analysis

All data were processed using GraphPad Prism 8.0. Flow cytometry was performed using FlowJoV10 software. The drawing materials for the illustrations in this article were created with BioRende. The details of the biological replicates and repetitions for each experiment are listed in the respective figure legends. All data are expressed as "mean ± standard deviation". Two groups were compared using two-tailed Student's *t* test, and multiple groups were compared using one-way analysis of variance (ANOVA) or two-way ANOVA, followed by multiple comparison test, as indicated in the figure legends. Statistical significance was set at $P < 0.05$.

Reporting summary

Further information on research design is available in the Nature Portfolio Reporting Summary linked to this article.

Data availability

Bulk RNA sequencing data generated in this study have been deposited in the Gene Expression Omnibus (GEO) database under accession codes GSE302900 and GSE302902. Single-cell RNA sequencing data are available in GEO under accession code GSE302903. Proteomics datasets (including protein microarray and Luminex liquid suspension array data) are included in the Additional Supplementary Files (Supplementary Data. 6, 7). The remaining data that support the findings of this study are available within the article, supplementary information, or Source Data file. Source data are provided with this paper.

References

1. Siegel, R. L., Miller, K. D., Wagle, N. S. & Jemal, A. Cancer statistics, 2023. *CA Cancer J. Clin.* **73**, 17–48 (2023).
2. Jones, R. P. et al. Colorectal liver metastases: a critical review of state of the art. *Liver Cancer* **6**, 66–71 (2016).
3. Katt, M. E., Wong, A. D. & Searson, P. C. Dissemination from a solid tumor: examining the multiple parallel pathways. *Trends Cancer* **4**, 20–37 (2018).
4. Liu, Y. & Cao, X. Characteristics and significance of the pre-metastatic niche. *Cancer Cell* **30**, 668–681 (2016).
5. Gavert, N. & Ben-Ze'ev, A. Epithelial-mesenchymal transition and the invasive potential of tumors. *Trends Mol. Med* **14**, 199–209 (2008).
6. Kitamura, T., Qian, B. Z. & Pollard, J. W. Immune cell promotion of metastasis. *Nat. Rev. Immunol.* **15**, 73–86 (2015).
7. Zhao, J. et al. Tumor-derived CXCL5 promotes human colorectal cancer metastasis through activation of the ERK/Elk-1/Snail and AKT/GSK3beta/beta-catenin pathways. *Mol. Cancer* **16**, 70 (2017).
8. Chen, C. et al. CXCL5 induces tumor angiogenesis via enhancing the expression of FOXD1 mediated by the AKT/NF-kappaB pathway in colorectal cancer. *Cell Death Dis.* **10**, 178 (2019).
9. Xia, J., Xu, X., Huang, P., He, M. & Wang, X. The potential of CXCL5 as a target for liver cancer - what do we know so far?. *Expert Opin. Ther. Targets* **19**, 141–146 (2015).
10. Eash, K. J., Greenbaum, A. M., Gopalan, P. K. & Link, D. C. CXCR2 and CXCR4 antagonistically regulate neutrophil trafficking from murine bone marrow. *J. Clin. Investig.* **120**, 2423–2431 (2010).
11. Zhou, S. L. et al. Overexpression of CXCL5 mediates neutrophil infiltration and indicates poor prognosis for hepatocellular carcinoma. *Hepatology* **56**, 2242–2254 (2012).
12. Haider, C. et al. Transforming Growth Factor-beta and Axl Induce CXCL5 and Neutrophil Recruitment in Hepatocellular Carcinoma. *Hepatology* **69**, 222–236 (2019).
13. Najjar, Y. G. et al. Myeloid-Derived Suppressor Cell Subset Accumulation in Renal Cell Carcinoma Parenchyma Is Associated with Intratumoral Expression of IL1beta, IL8, CXCL5, and Mip-1alpha. *Clin. Cancer Res.* **23**, 2346–2355 (2017).
14. Spiegel, A. et al. Neutrophils suppress intraluminal NK cell-mediated tumor cell clearance and enhance extravasation of disseminated carcinoma cells. *Cancer Discov.* **6**, 630–649 (2016).

15. Szczerba, B. M. et al. Neutrophils escort circulating tumour cells to enable cell cycle progression. *Nature* **566**, 553–557 (2019).
16. Shaul, M. E. & Fridlender, Z. G. Tumour-associated neutrophils in patients with cancer. *Nat. Rev. Clin. Oncol.* **16**, 601–620 (2019).
17. Xiao, Y. et al. Cathepsin C promotes breast cancer lung metastasis by modulating neutrophil infiltration and neutrophil extracellular trap formation. *Cancer Cell* **39**, 423–437 e427 (2021).
18. Lee, W. et al. Neutrophils facilitate ovarian cancer premetastatic niche formation in the omentum. *J. Exp. Med.* **216**, 176–194 (2019).
19. Wculek, S. K. & Malanchi, I. Neutrophils support lung colonization of metastasis-initiating breast cancer cells. *Nature* **528**, 413–417 (2015).
20. Albrengues, J. et al. Neutrophil extracellular traps produced during inflammation awaken dormant cancer cells in mice. *Science* **361**, https://doi.org/10.1126/science.aao4227 (2018).
21. Di Carlo, E. et al. The intriguing role of polymorphonuclear neutrophils in antitumor reactions. *Blood* **97**, 339–345 (2001).
22. Granot, Z. et al. Tumor entrained neutrophils inhibit seeding in the premetastatic lung. *Cancer Cell* **20**, 300–314 (2011).
23. Linde, I. L. et al. Neutrophil-activating therapy for the treatment of cancer. *Cancer Cell* **41**, 356–372 e310 (2023).
24. Cui, C. et al. Neutrophil elastase selectively kills cancer cells and attenuates tumorigenesis. *Cell* **184**, 3163–3177 e3121 (2021).
25. Adrover, J. M., McDowell, S. A. C., He, X. Y., Quail, D. F. & Egeblad, M. NETworking with cancer: the bidirectional interplay between cancer and neutrophil extracellular traps. *Cancer Cell* **41**, 505–526 (2023).
26. Sagiv, J. Y. et al. Phenotypic diversity and plasticity in circulating neutrophil subpopulations in cancer. *Cell Rep.* **10**, 562–573 (2015).
27. Park, J. et al. Cancer cells induce metastasis-supporting neutrophil extracellular DNA traps. *Sci. Transl. Med* **8**, 361ra138 (2016).
28. Steele, C. W. et al. CXCR2 inhibition profoundly suppresses metastases and augments immunotherapy in pancreatic ductal adenocarcinoma. *Cancer Cell* **29**, 832–845 (2016).
29. Teijeira, A. et al. CXCR1 and CXCR2 chemokine receptor agonists produced by tumors induce neutrophil extracellular traps that interfere with immune cytotoxicity. *Immunity* **52**, 856–871 e858 (2020).
30. Casanova-Acebes, M. et al. Neutrophils instruct homeostatic and pathological states in naive tissues. *J. Exp. Med* **215**, 2778–2795 (2018).
31. Fuchs, T. A. et al. Novel cell death program leads to neutrophil extracellular traps. *J. Cell Biol.* **176**, 231–241 (2007).
32. Condamine, T. et al. Lectin-type oxidized LDL receptor-1 distinguishes population of human polymorphonuclear myeloid-derived suppressor cells in cancer patients. *Sci. Immunol.* **1**, https://doi.org/10.1126/sciimmunol.aaf8943 (2016).
33. Cao, Z. et al. Establishment of a stable hepatic metastasis mouse model of murine colorectal cancer by microsurgical orthotopic implantation. *Transl. Cancer Res.* **9**, 3249–3257 (2020).
34. Zhu, Y. P. et al. CyTOF mass cytometry reveals phenotypically distinct human blood neutrophil populations differentially correlated with melanoma stage. *J. Immunother. Cancer* **8**, https://doi.org/10.1136/jitc-2019-000473 (2020).
35. Liu, S. et al. The evolution and heterogeneity of neutrophils in cancers: origins, subsets, functions, orchestrations and clinical applications. *Mol. Cancer* **22**, 148 (2023).
36. Xue, R. et al. Liver tumour immune microenvironment subtypes and neutrophil heterogeneity. *Nature* **612**, 141–147 (2022).
37. Salcher, S. et al. High-resolution single-cell atlas reveals diversity and plasticity of tissue-resident neutrophils in non-small cell lung cancer. *Cancer Cell* **40**, 1503–1520 e1508 (2022).
38. Zilionis, R. et al. Single-cell transcriptomics of human and mouse lung cancers reveals conserved myeloid populations across individuals and species. *Immunity* **50**, 1317–1334 e1310 (2019).
39. Luca, B. A. et al. Atlas of clinically distinct cell states and ecosystems across human solid tumors. *Cell* **184**, 5482–5496 e5428 (2021).
40. Wang, L. et al. Single-cell RNA-seq analysis reveals BHLHE40-driven pro-tumour neutrophils with hyperactivated glycolysis in pancreatic tumour microenvironment. *Gut* **72**, 958–971 (2023).
41. Amulic, B., Cazalet, C., Hayes, G. L., Metzler, K. D. & Zychlinsky, A. Neutrophil function: from mechanisms to disease. *Annu. Rev. Immunol.* **30**, 459–489 (2012).
42. Korkmaz, B., Horwitz, M. S., Jenne, D. E. & Gauthier, F. Neutrophil elastase, proteinase 3, and cathepsin G as therapeutic targets in human diseases. *Pharm. Rev.* **62**, 726–759 (2010).
43. Burn, G. L., Foti, A., Marsman, G., Patel, D. F. & Zychlinsky, A. The neutrophil. *Immunity* **54**, 1377–1391 (2021).
44. Bakrim, S. et al. Targeting inflammation in cancer therapy: from mechanistic insights to emerging therapeutic approaches. *J. Transl. Med.* **23**, 588 (2025).
45. Yipp, B. G. et al. Infection-induced NETosis is a dynamic process involving neutrophil multitasking in vivo. *Nat. Med.* **18**, 1386–1393 (2012).
46. Liang, W., Li, Q. & Ferrara, N. Metastatic growth instructed by neutrophil-derived transferrin. *Proc. Natl. Acad. Sci. USA* **115**, 11060–11065 (2018).
47. Morris, G., Gevezova, M., Sarafian, V. & Maes, M. Redox regulation of the immune response. *Cell Mol. Immunol.* **19**, 1079–1101 (2022).
48. Kim, K., Li, J., Tseng, A., Andrews, R. K. & Cho, J. NOX2 is critical for heterotypic neutrophil-platelet interactions during vascular inflammation. *Blood* **126**, 1952–1964 (2015).
49. Douda, D. N., Khan, M. A., Grasemann, H. & Palaniyar, N. SK3 channel and mitochondrial ROS mediate NADPH oxidase-independent NETosis induced by calcium influx. *Proc. Natl. Acad. Sci. USA* **112**, 2817–2822 (2015).
50. Xu, J. et al. NLRC3 expression in macrophage impairs glycolysis and host immune defense by modulating the NF-kappaB-NFAT5 complex during septic immunosuppression. *Mol. Ther.* **31**, 154–173 (2023).
51. Han, E. J. et al. Suppression of NFAT5-mediated inflammation and chronic arthritis by novel kappab-binding inhibitors. *EBioMedicine* **18**, 261–273 (2017).
52. Munder, M. et al. Suppression of T-cell functions by human granulocyte arginase. *Blood* **108**, 1627–1634 (2006).
53. Thiam, H. R., Wong, S. L., Wagner, D. D. & Waterman, C. M. Cellular mechanisms of NETosis. *Annu. Rev. Cell Dev. Biol.* **36**, 191–218 (2020).
54. Papayannopoulos, V., Metzler, K. D., Hakkim, A. & Zychlinsky, A. Neutrophil elastase and myeloperoxidase regulate the formation of neutrophil extracellular traps. *J. Cell Biol.* **191**, 677–691 (2010).
55. Yuzhalin, A. E. et al. Colorectal cancer liver metastatic growth depends on PAD4-driven citrullination of the extracellular matrix. *Nat. Commun.* **9**, 4783 (2018).
56. Fridlender, Z. G. et al. Polarization of tumor-associated neutrophil phenotype by TGF-beta: "N1" versus "N2" TAN. *Cancer Cell* **16**, 183–194 (2009).
57. Li, M. O. et al. Innate immune cells in the tumor microenvironment. *Cancer Cell* **39**, 725–729 (2021).
58. Alshetaiwi, H. et al. Defining the emergence of myeloid-derived suppressor cells in breast cancer using single-cell transcriptomics. *Sci. Immunol.* **5**, https://doi.org/10.1126/sciimmunol.aay6017 (2020).
59. Martinez Sanz, P. et al. G-CSF as a suitable alternative to GM-CSF to boost dinutuximab-mediated neutrophil cytotoxicity in neuroblastoma treatment. *J. Immunother. Cancer* **9**, https://doi.org/10.1136/jitc-2020-002259 (2021).

60. Huang, M. et al. New insights into antiangiogenic therapy resistance in cancer: mechanisms and therapeutic aspects. *Drug Resist. Updat.* **64**, 100849 (2022).
61. Burnet, F. M. The concept of immunological surveillance. *Prog. Exp. Tumor Res.* **13**, 1–27 (1970).
62. Dunn, G. P., Bruce, A. T., Ikeda, H., Old, L. J. & Schreiber, R. D. Cancer immunoediting: from immunosurveillance to tumor escape. *Nat. Immunol.* **3**, 991–998 (2002).
63. Guc, E. & Pollard, J. W. Redefining macrophage and neutrophil biology in the metastatic cascade. *Immunity* **54**, 885–902 (2021).
64. Cools-Lartigue, J. et al. Neutrophil extracellular traps sequester circulating tumor cells and promote metastasis. *J. Clin. Investig.* **123**, 3446–3458 (2013).
65. Li, P. et al. Lung mesenchymal cells elicit lipid storage in neutrophils that fuel breast cancer lung metastasis. *Nat. Immunol.* **21**, 1444–1455 (2020).
66. Yang, L. et al. DNA of neutrophil extracellular traps promotes cancer metastasis via CCDC25. *Nature* **583**, 133–138 (2020).
67. Gong, Z. et al. Immunosuppressive reprogramming of neutrophils by lung mesenchymal cells promotes breast cancer metastasis. *Sci. Immunol.* **8**, eadd5204 (2023).
68. Chao, T., Furth, E. E. & Vonderheide, R. H. CXCR2-dependent accumulation of tumor-associated neutrophils regulates T-cell immunity in pancreatic ductal adenocarcinoma. *Cancer Immunol. Res.* **4**, 968–982 (2016).
69. Jones-Bolin, S. Guidelines for the care and use of laboratory animals in biomedical research. *Curr. Protoc. Pharmacol.* Appendix 4, Appendix 4B, https://doi.org/10.1002/0471141755.pha04bs59 (2012).
70. Ye, C. et al. DRUG-seq for miniaturized high-throughput transcriptome profiling in drug discovery. *Nat. Commun.* **9**, 4307 (2018).
71. Wu, Y. et al. Neutrophil profiling illuminates anti-tumor antigen-presenting potency. *Cell* **187**, 1422–1439 e1424 (2024).
72. Dura, B. et al. scFTD-seq: freeze-thaw lysis based, portable approach toward highly distributed single-cell 3′ mRNA profiling. *Nucleic Acids Res.* **47**, e16 (2019).
73. Hao, Y. et al. Integrated analysis of multimodal single-cell data. *Cell* **184**, 3573–3587 e3529 (2021).
74. Bergen, V., Lange, M., Peidli, S., Wolf, F. A. & Theis, F. J. Generalizing RNA velocity to transient cell states through dynamical modeling. *Nat. Biotechnol.* **38**, 1408–1414 (2020).
75. Ashburner, M. et al. Gene ontology: tool for the unification of biology. The Gene Ontology Consortium. *Nat. Genet.* **25**, 25–29 (2000).
76. Xu, Z. et al. CCL7 and TGF-beta secreted by MSCs play opposite roles in regulating CRC metastasis in a KLF5/CXCL5-dependent manner. *Mol. Ther.* **30**, 2327–2341 (2022).
77. Shen, X. et al. KLF5 inhibition overcomes oxaliplatin resistance in patient-derived colorectal cancer organoids by restoring apoptotic response. *Cell Death Dis.* **13**, 303 (2022).
78. Schnalzger, T. E. et al. 3D model for CAR-mediated cytotoxicity using patient-derived colorectal cancer organoids. *EMBO J.* **38**, https://doi.org/10.15252/embj.2018100928 (2019).
79. Li, W. et al. Cytokine concentration in peripheral blood of patients with colorectal cancer. *Front. Immunol.* **14**, 1175513 (2023).
80. Fendler, A. et al. Inhibiting WNT and NOTCH in renal cancer stem cells and the implications for human patients. *Nat. Commun.* **11**, 929 (2020).

Acknowledgements

This study was supported by National Natural Science Foundation of China (81871933 (A.L.), 81802326 (J.Z.), 82003169 (H.F.), 82403528 (Zq.X.)), Foundation of Shanghai Municipal Health Committee (202040144 (Yp.Z.)), and the Shanghai Science and Technology Innovation Action Plan (24YF2711100 (Zq.X.)). Schematic diagrams were created using BioRender.com. We thank Guo, Z. and ZHENG, F. for technical assistance and discussion. We would like to thank Editage (www.editage.cn) for English language editing.

Author contributions

Conceptualization, J.Z. and A.L.; Methodology, Zf.X., H.F. and J.Z.; Investigation, Zq.X., H.F., Yc.Z., Wy.L., A.T., S.Y. and Z.L.; Formal Analysis, F.C. and X.C.; Writing – Original Draft, Zq.X., H.G. and J.H.; Writing – Review & Editing, W.F., Yp.Z., X.C. and X.S.; Writing – Revised Draft, Zq.X., H.F., Yc.Z. and X.C.; Funding Acquisition, X.C. and A.L.; Project Administration, X.S. and Yp.Z.; Resources, W.F. and Wc.L.; Supervision, X.S. and A.L.

Competing interests

The authors declare no competing interests.

Additional information

Supplementary information The online version contains supplementary material available at https://doi.org/10.1038/s41467-025-67579-7.

Correspondence and requests for materials should be addressed to Xiaohui Shen, Xi Cheng, Jingkun Zhao or Aiguo Lu.

Peer review information *Nature Communications* thanks anonymous reviewer(s) for their contribution to the peer review of this work. A peer review file is available.